

AD-A112 185 NATIONAL BUREAU OF STANDARDS WASHINGTON DC NATIONAL M--ETC F/G 7/4
PASSIVE FILMS, SURFACE STRUCTURE AND STRESS CORROSION AND CREVI--ETC(U)
AUG 80 J KRUGER, J J CARROLL, A J MELMED NAONR-18-89

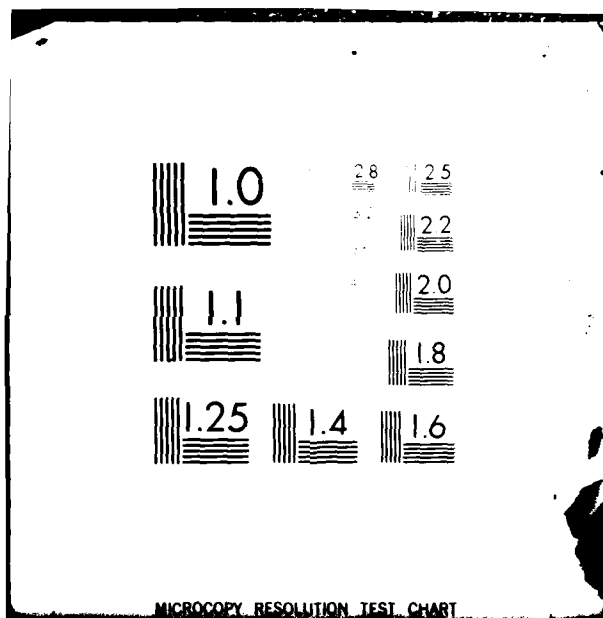
NATIONAL BUREAU OF STANDARDS WASHINGTON DC NATIONAL M--ETC F/G 7/4
PASSIVE FILMS, SURFACE STRUCTURE AND STRESS CORROSION AND CREVI--ETC(U)
AUG 80 J KRUGER, J J CARROLL, A J MELMED NAONR-18-89

UNCLASSIFIED

• NEL

1 OF 1
AD A
11/2/94

END
DATE
FILMED
04-82
DTIC



NBSIR (Navy)

Passive Films, Surface Structure and Stress Corrosion and Crevice Corrosion Susceptibility

200-1
DDO 50
PAC.

J. Kruger, J. J. Carroll, A. J. Melmed
J. J. Ritter,

Chemical Stability and Corrosion Division
and
Surface Science Division
National Bureau of Standards
U.S. Department of Commerce
Washington, D.C. 20234

August 1980

Technical Summary Report No. 10

Prepared for
Office of Naval Research
Department of the Navy
Arlington, VA 22217

DEC 1980
MAR 19 1982
S A

This document has been approved
for public release and sale; its
distribution is unlimited.

82 03 05 023

ADA112185

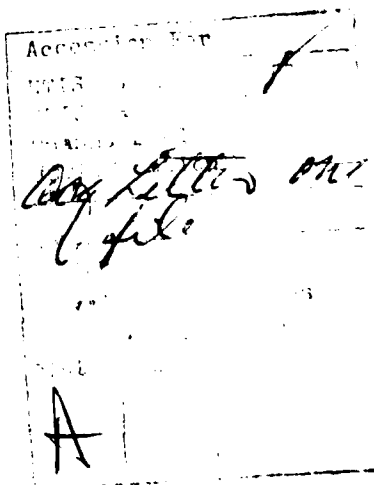
DTIC FILE COPY

A Qualitative Ellipsometric-Electrochemical Approach
for the Study of Film Growth Under Organic Coatings

J. J. Ritter and J. Kruger
National Measurement Laboratory
Center for Materials Science
National Bureau of Standards
Washington, D.C. 20234

Abstract

A feasibility study was made to determine if qualitative ellipsometry can be used together with electrochemical pH and potential measurements as a technique for the study of metal substrates protected by transparent organic coatings. The objective of the work was to gain a deeper understanding of the mechanisms governing the corrosion protective actions of paints on metal surfaces. Computer modeling and experiments with collodion coatings on iron substrates indicated that changes in the ellipsometric parameter Δ could, for the most part, be safely interpreted as thickness alterations in the substrate oxide film. Experiments with the Fe-collodion system in dilute chloride solutions exhibited three sequential stages of activity, two of which could be interpreted in terms of corrosion mechanisms using the optical and electrochemical measurements. Chromate ion as a corrosion inhibitor in coatings was also studied using this technique, and was shown to have significant effects upon the development of the sub-coating processes.



A Qualitative Ellipsometric-Electrochemical Approach
for the Study of Film Growth Under Organic Coatings

J. J. Ritter and J. Kruger
National Measurement Laboratory
Center for Materials Science
National Bureau of Standards
Washington, D.C. 20234

A recent book [1] Corrosion Control by Coatings gives examples of many areas where there is still a great lack of understanding of the processes that control the corrosion protection actions of paints. Of special value for addressing this need would be a technique or techniques that could carry out in situ studies of the growth and dissolution of the oxide films and other films that exist on a metal surface covered by a paint and how changes in the composition of the paint affects these films. Also of great value would be a technique that could detect changes in the organic coating that constitutes the paint, changes in the environment that develops under the coating, and finally how such changes lead to the delamination processes that result in detachment of the paint from the oxide covered metal surface.

This paper presents a description of the first attempts to evaluate whether ellipsometry can serve as a tool for examining the processes that occur under paint films. The approach simulates the painted metal circumstance by using a transparent organic coating deposited on a metal surface. Particles of solid chemicals (e.g., chromates) can be placed around the ellipsometer observation region and under the coating in simulation of corrosion inhibitors found in paint formulations. These dissolve slowly and modify the environment under the organic coating. A pH probe, located under the coating and at the metal surface, allows monitoring of the sub-coating environment.

Obviously, such a system is too complicated to permit rigorous quantitative ellipsometric determination of film or environmental optical constants or film thicknesses. Instead, the approach employed in the work described here is the qualitative one described in the Third International Conference on Ellipsometry [2]. This approach measures the time dependence of changes which occur as indicated by significant alterations in Δ , ψ and correlates these changes with concomitant electrochemical measurements. Thus, for example, the rate of change of film thickness (assumed proportional to Δ) can be monitored. To help interpret the changes of Δ and ψ observed, and to judge whether the magnitude and direction are realistic and reasonable, model calculations using the Drude equations and reasonable optical parameters were carried out.

An extension of this work will include repassivation rate studies in simulated sub-coating environments by the triboellipsometric technique [3].

EXPERIMENTAL

Metallic specimens were cast in epoxy resin and polished on a series of successively finer abrasives, the final abrasive being 0.05 μm aluminum oxide. The iron specimens were provided with a Pt wire electrode and an opening to accomodate a commercial 1.5 mm dia. pH microprobe, as shown in Fig. 1. During the coating process, the pH probe opening was closed with a snug fitting polytetrafluoroethylene (PTFE) plug to assure the formation of a monolithic coating across the entire face of the specimen and mount. In general, collodion (cellulose dinitrate) and methanol were mixed 1:1 on a volume basis and the specimen face coated by dipping. The coated specimens were air dried for about 0.5 h and subjected to a vacuum curing at about 10^{-3} torr for 1.5 h. Cured coatings with thickness ranging from 0.01 to 0.03 mm were obtained in this manner.

For some experiments, a suspension of finely ground K_2CrO_4 in methanol was placed dropwise directly on the polished iron surface. The evaporation of solvent left "islands" of K_2CrO_4 (Cf. Fig. 2) which were then coated over by dipping the specimen in a 1:1 collodion-methanol mixture. After the vacuum curing step, the PTFE plug was extracted from the rear of the specimen mount and the micro pH probe installed so that it just touched the underside of the coating. The probe lead wire was sealed to the rear of epoxy mount with a small quantity of vacuum putty.

Prepared specimens were mounted vertically and optically aligned in a PTFE-lined cell. Reference electrodes for the electrochemical measurements were connected to the system through Luggin capillary salt bridges set in the bulk solution. Zero time for the experiments was taken at the moment of specimen immersion in 0.05 N NaCl solution.

Infrared spectra of the coatings on the specimens before and after immersion were obtained by reflectance techniques using a commercial double beam infrared spectrophotometer.

Specimens were maintained at open circuit potential which was measured with respect to a saturated calomel electrode and reported with respect to a standard H_2 electrode.

Computer modeling was done on the basis of a three film system with the estimated parameters shown in Fig. 3. The multiple film portion of a computer program for ellipsometry was utilized for the computations [4].

RESULTS AND DISCUSSION

Computer Modeling

The results of computer modeling as illustrated in Figs. 4 and 5 allow the determination of both the direction and the relative orders of magnitude

of the changes in Δ and ψ to be expected for the three film system. It is readily seen from a comparison of $\frac{\delta\Delta}{\delta d}$ and $\frac{\delta\psi}{\delta d}$ values that Δ is a factor of ten more responsive to changes in the oxide film thickness (d_3) than to changes in the liquid film thickness (d_2). Moreover, an increase in either d_2 or d_3 results in a decrease in both Δ and ψ .

Collodion Coating on Gold

Ellipsometric measurements were made on polished gold to determine whether significant optical changes can be expected when it is immersed in aqueous 0.05 N NaCl. Random fluctuations of Δ and ψ of the order of only $\pm 0.2^\circ$ over a period of 1400 min were observed and indicated that minimal contributions to changes in Δ and ψ would arise from the gold surface. The same specimen coated with collodion showed a decrease in Δ values ($\sim 1^\circ$) over a 1800 min period, while ψ remained essentially constant as illustrated in Fig. 6. The reflectance infrared spectra of the collodion before and after the extended immersion in the chloride medium were essentially identical. The observed decrease in Δ is probably due to the development of a liquid film under the coating and is consistent with the computer modeling results. The thickness of this liquid film, d_2 , is estimated at about 3 nm on the basis of computer modeling.

Thus, the work with the relatively inert gold surfaces in dilute Cl^- media shows the magnitude of the ellipsometric changes which arise from the collodion and the formation of a liquid film under the collodion. These changes, as is apparent from Fig. 6, are small and can be readily accounted for in experiments with iron substrates.

Collodion Coating on Iron

Fig. 7 indicates that on the basis of changes in Δ , the Fe-collodion system proceeds through three distinct stages. During the first 1000 min.,

Δ rises gradually, ψ decreases as does ϕ_{Fe} . The pH increases during this period. The next stage covering from 1000 to 6000 min. shows a considerable decline in Δ ($\sim 25^\circ$) concomitant with a continued decrease in ψ , ϕ_{Fe} . The pH tends to higher and higher values. In the third stage, Δ undergoes a series of reversals, while ψ and pH increase. By 5400 min. an anodic area was well developed at the upper corner of the specimen, and remote from the pH probe and ellipsometer observation regions.

On the basis of computer modeling, the first stage of the experiment where Δ increases and ψ decreases is difficult to reconcile with reasonable events thought to occur under the organic coating. One set of conditions which does predict the divergence of Δ and ψ as observed is the formation of a liquid film combined with an increase of the liquid film index (n_2) and a radical decrease in \hat{n}_3 for the oxide film. This would suggest a substantive change in either the chemical composition or the molecular and/or atomic arrangement of the existing oxide film. The possibilities here will be explored using the derivative plot in n, k space approach developed at NBS by Melmed and Carroll [5].

The second stage with a significant decrease in Δ and ψ probably represents the growth of an oxide film on the substrate of the order of 15 nm in thickness. The interpretation of events in this stage is quite reasonable in view of the sub-coating pH and specimen potential which comprise very favorable conditions for the formation of Fe_2O_3 .

Several events may be occurring in the final stage. The pH and potential at this point are favorable for the dissolution of Fe and its stabilization as the FeO_4^{-2} ion. The first of these would result in surface roughening,

while the second would lead to an optically absorbing liquid film since the ion is colored. Additional experiments and more sophisticated computer modeling are required to correlate the observed changes in Δ and ψ to events in this stage.

Collodion Coating on Iron with K_2CrO_4 Islands

Fig. 8 shows the first stage of the experiment lasts about 1200 min. and indicates both Δ and ψ decreasing. The change in Δ is reminiscent of the changes seen for the gold-collodion system and may simply represent the accretion of liquid under the coating. The concomitant decrease in ψ is consistent with this interpretation, but the magnitude of the change is not as readily explained and must await additional experiments.

The second stage of the process is notably different from previous experiments in that the decrease in Δ is of the order of only 2° as compared to the 25° change seen with the previous system. It appears that the CrO_4^{-2} greatly inhibits film growth in this stage.

Evidence for a third stage is absent, suggesting an inhibition of the metal dissolution process.

During the experiment, the pH rises to about 10, levels off and finally fluctuates between 9.3 and 10. This signifies some attenuation of the corrosion process and is consistent with the expectations for the effect of chromate inhibitor. After 9800 min. immersion, the chromate islands were nearly obliterated, and three separate and very small anodic regions remote from the pH probe and optical region were noted on the surface.

In general, the presence of the chromate "islands" markedly alters both the first and second stages of the sub-coating-processes while eliminating the third stage altogether within the time frame examined.

CONCLUDING COMMENTS

The main objective of this work was to explore the feasibility of using a qualitative ellipsometric approach as a tool for obtaining a better understanding of the corrosion processes occurring under organic coatings. The results described in the prior section indicate that even in its rudimentary stage, an ellipsometric examination of corrosion processes under coatings can provide useful information hitherto not available from previously tried methods of study. It has been shown using this technique that:

- 1) It is possible to identify three different stages occurring during the first 10^4 minutes with the collodion coating system used in this study. Moreover, one can begin to correlate these optically measured stages with time, pH and potential measurements.
- 2) It is possible to develop reasonable and consistent (consistency between optical, pH and potential measurements) interpretations of the processes occurring in the second and third stages but not for the first.
- 3) It is possible to interpret the effect of the addition of inhibitory chemicals on the processes observed and to consider them with respect to measurements of repassivation kinetics.
Repassivation kinetic studies of iron in simulated sub-coating environments using the triboellipsometric technique [3] are in progress and will be the subject of a future publication.

Thus, while much remains to be done to refine both the experimental and interpretive approaches (for example, the paper by Theeten, et al [6] suggest the possibility that variation of λ may help), this feasibility study has shown that the application of qualitative ellipsometry to the study of the corrosion processes under organic coatings shows considerable promise.

ACKNOWLEDGEMENTS

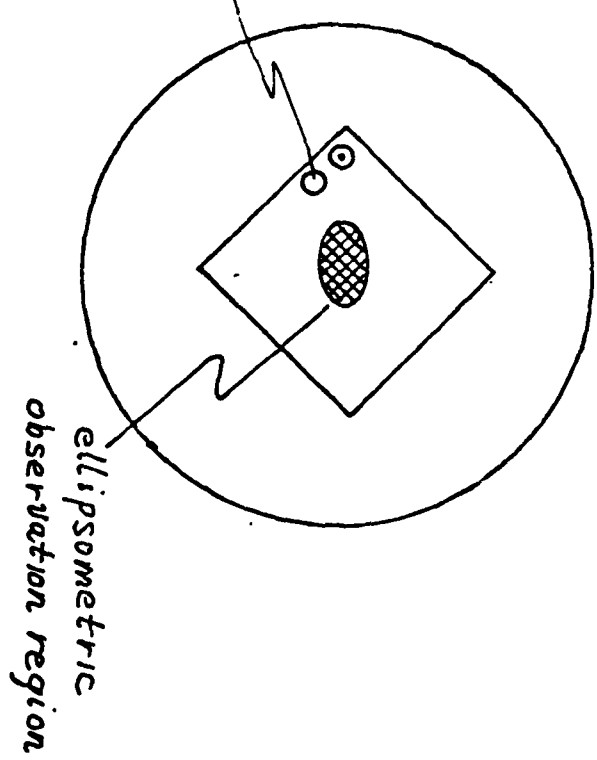
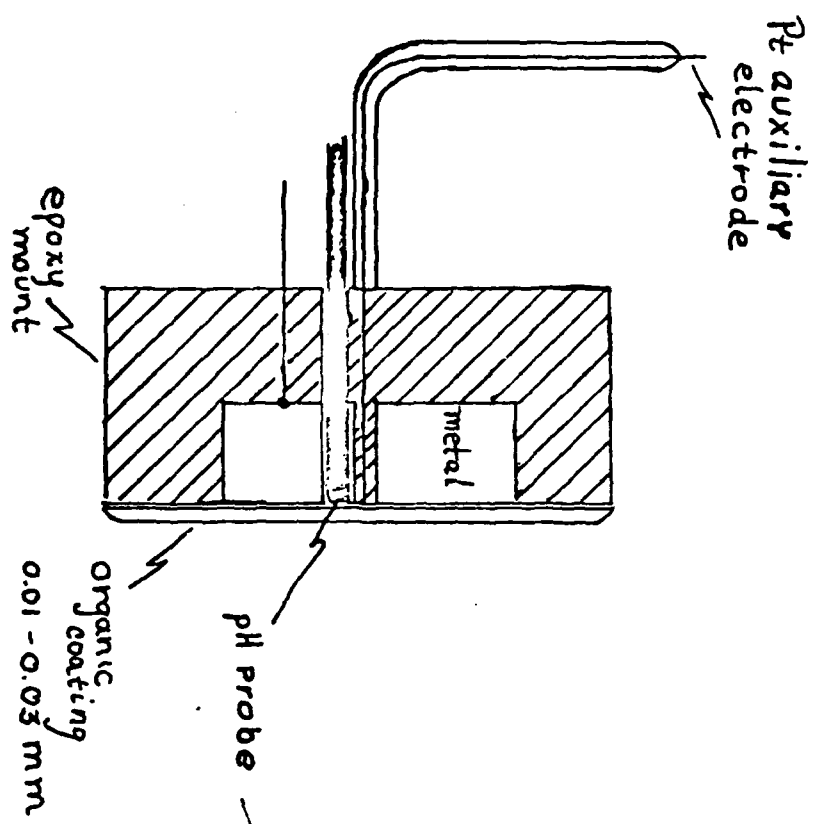
We are most grateful to the Office of Naval Research, which supported this work under Contract NACNR 18-89 MRO 36-082.

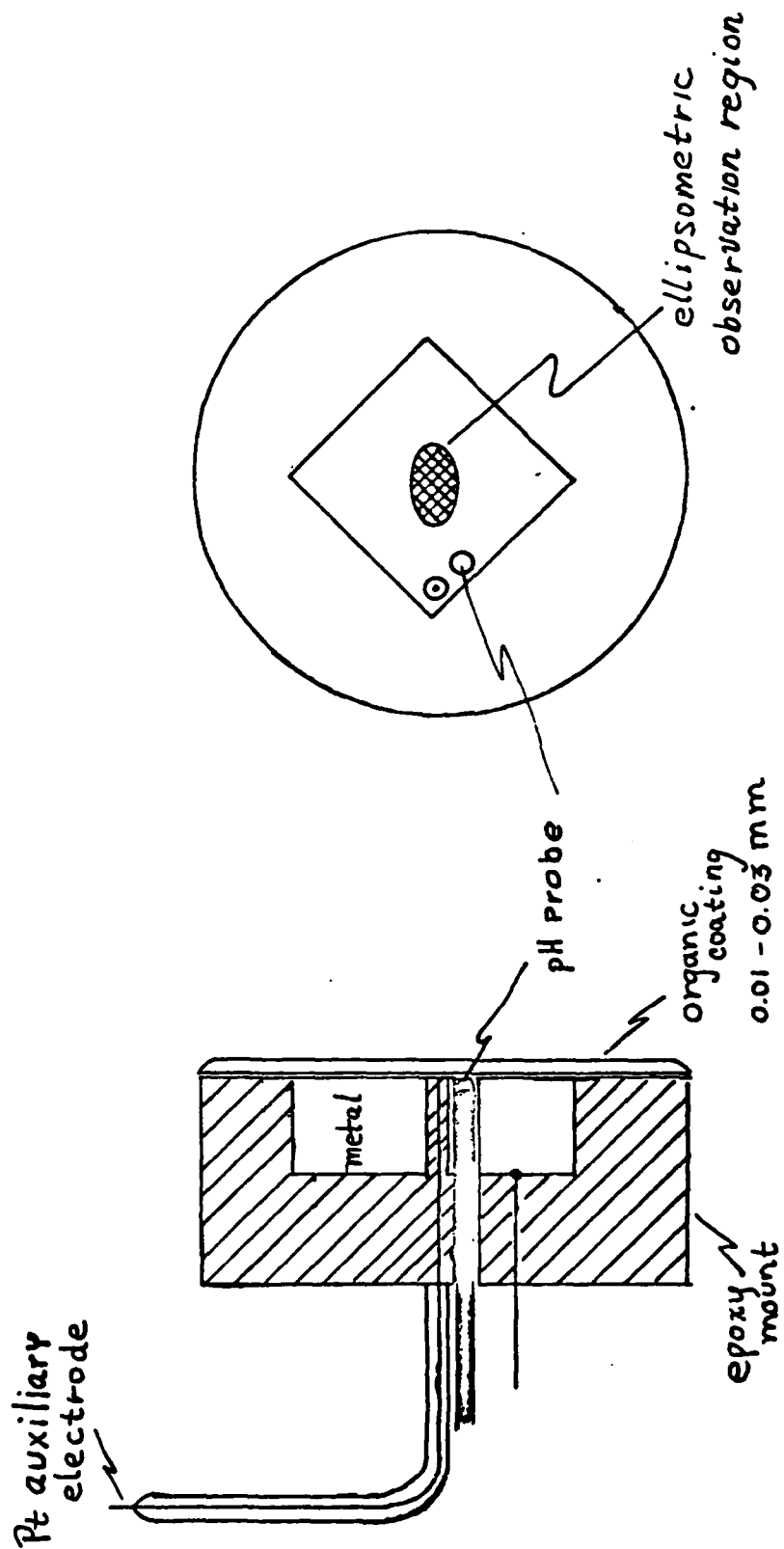
FIGURE CAPTIONS

1. Details of the mounted iron specimen.
2. Mounted iron specimen showing location of chromate islands.
3. Three film system and parameters for computer modeling.
4. Results of computer modeling of rate of change of Δ and ψ for fixed oxide film ($d_3 = 3$ nm) and variable liquid film, d_2 .
5. Results of computer modeling of rate of change of Δ and ψ for a fixed liquid film ($d_2 = 5$ nm) and a variable oxide film, d_3 .
6. Δ and ψ vs. time for Au with collodion in 0.05 N NaCl.
7. Δ , ψ , pH and ϕ_{Fe} vs. time for Fe with collodion in 0.05 N NaCl.
8. Δ , ψ , pH and ϕ_{Fe} vs. time for Fe with collodion and CrO_4^{-2} islands in 0.05 N NaCl.

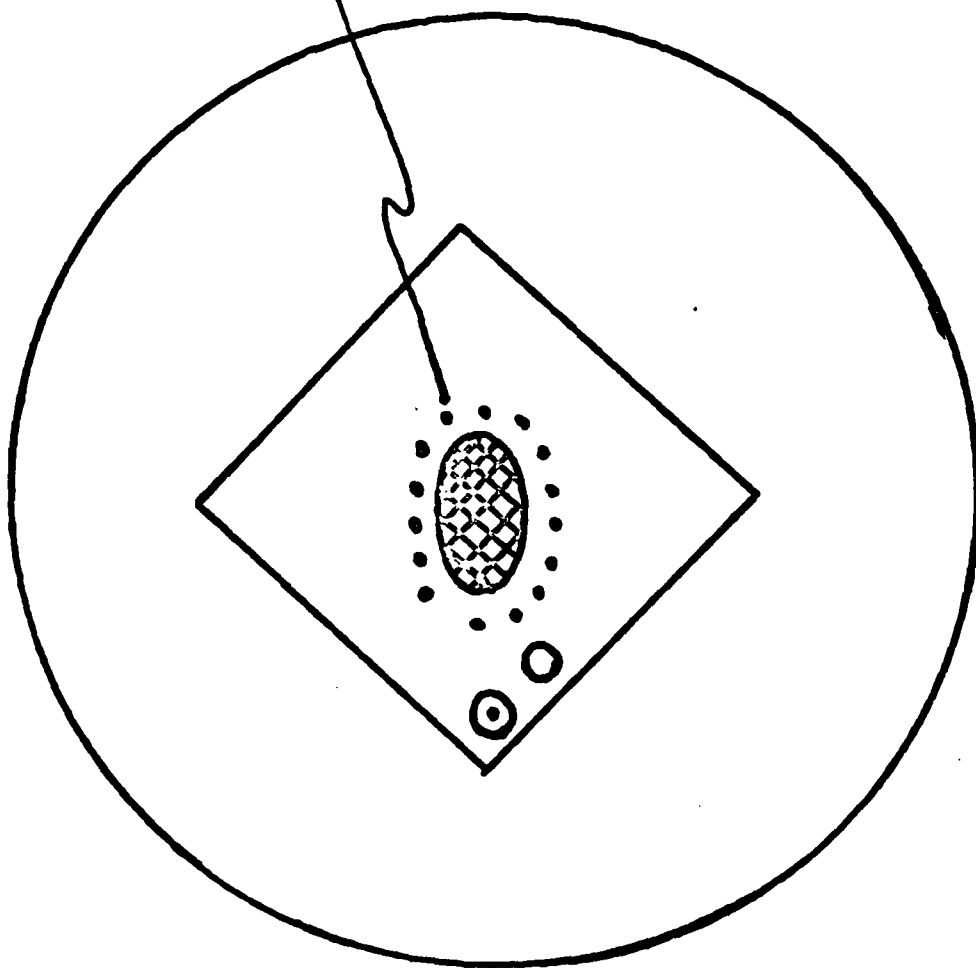
REFERENCES

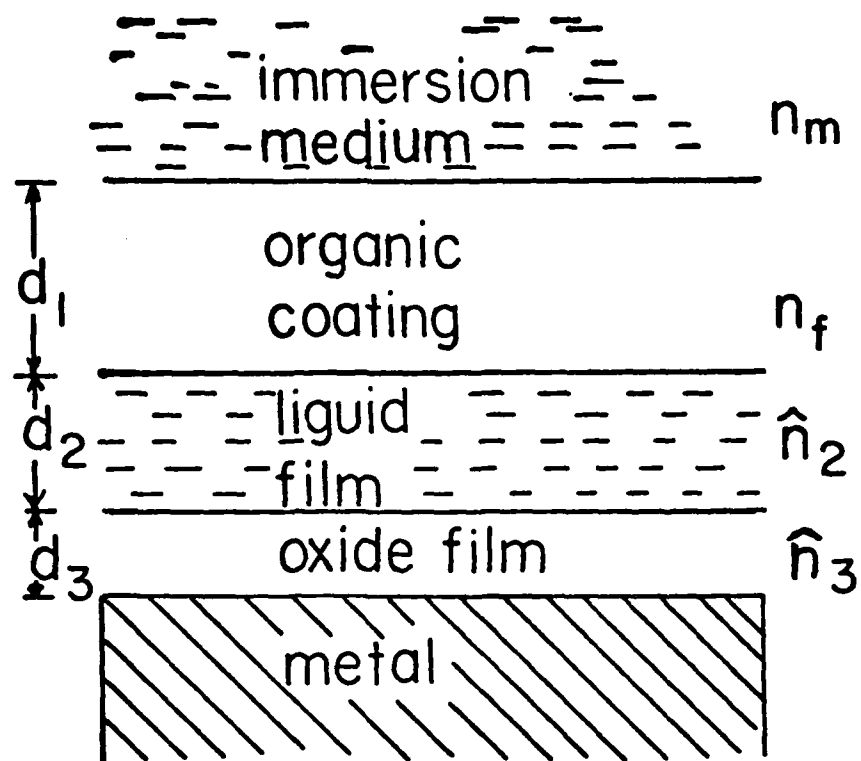
- [1] Corrosion Control by Coatings, H. Leidheiser, Jr., ed., Science Press, Princeton, 1979.
- [2] J. Kruger and J. R. Ambrose, Surf. Sci., 56, (1976), 394.
- [3] J. R. Ambrose and J. Kruger, Corrosion, 28, (1971), 30.
- [4] F. L. McCrackin, "A Fortran Program for Analysis of Ellipsometer Measurements", NBS Technical Note 479 (1969).
- [5] A. J. Melmed and J. J. Carroll, this Conference.
- [6] J. B. Theeten, D. E. Aspenes and R. R. H. Chang, J. Appl. Phys., 49 (1978), 6097.





CHROMATE
ISLANDS



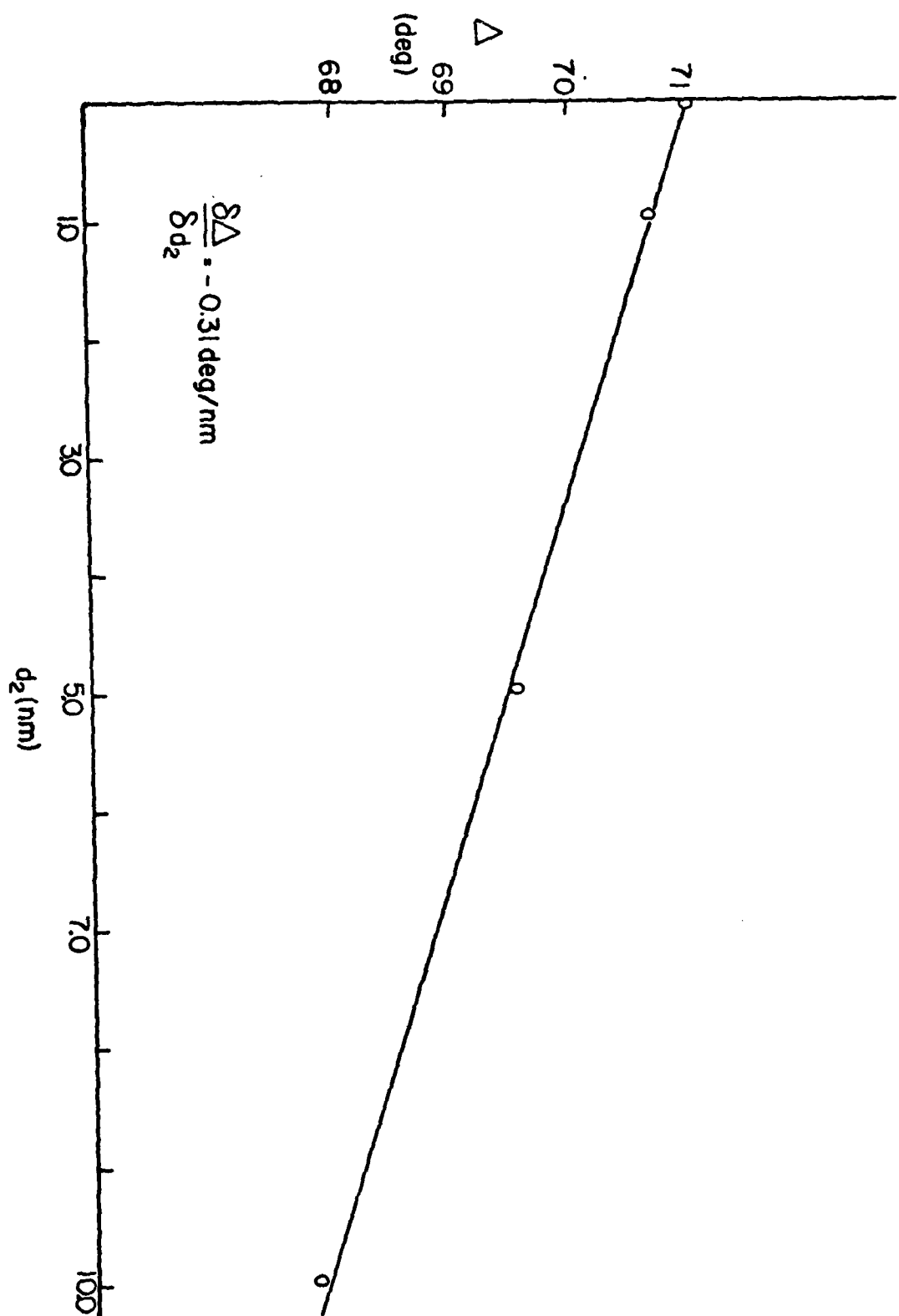


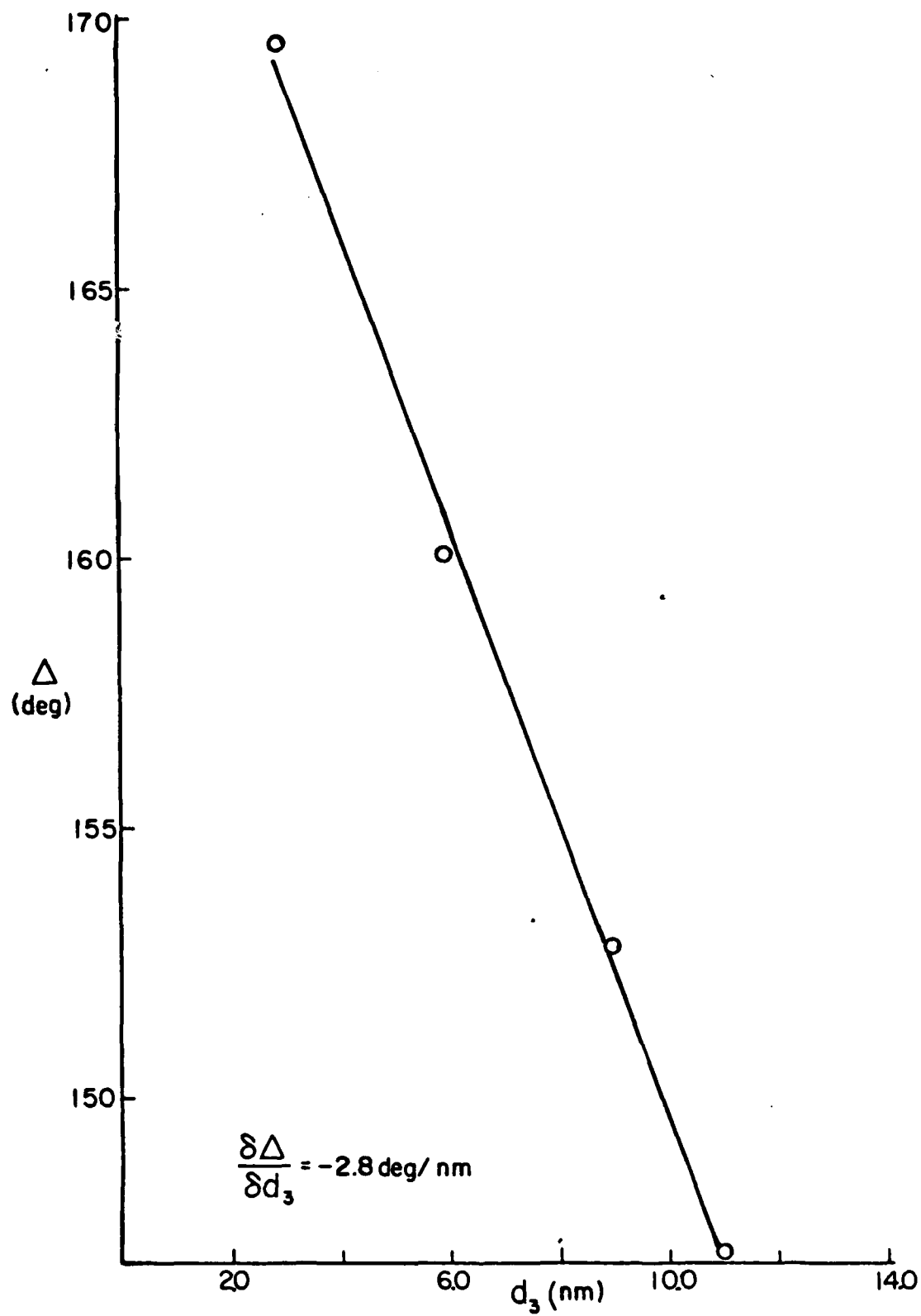
	n	K
IMMERSION MEDIUM	1.33	0
ORGANIC COATING	1.45	0
LIQUID FILM	1.40	0
OXIDE FILM	2.5	0.12
SUBSTRATE	3.35	1.15

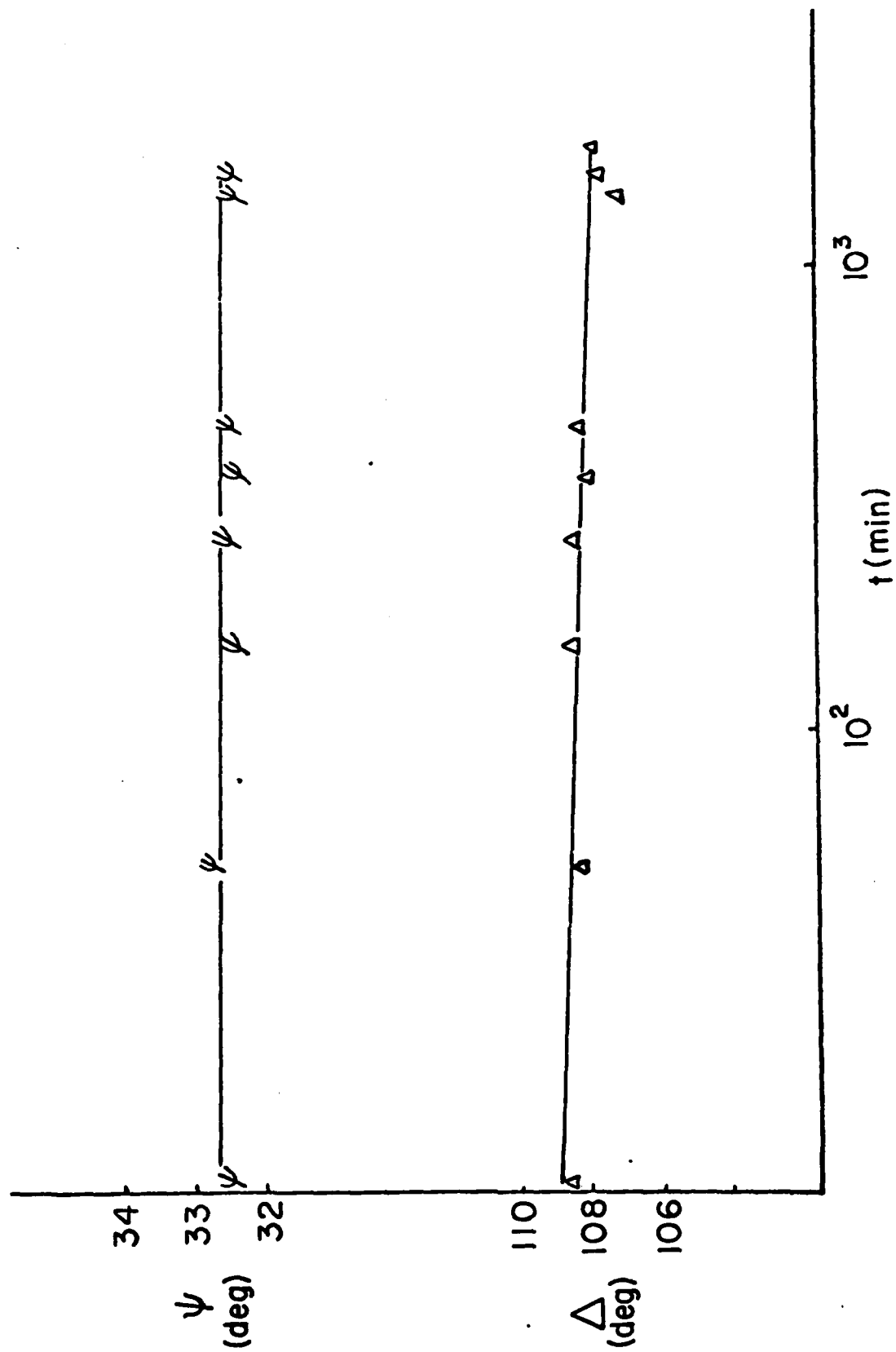
$$\hat{n} = n(1 - iK)$$

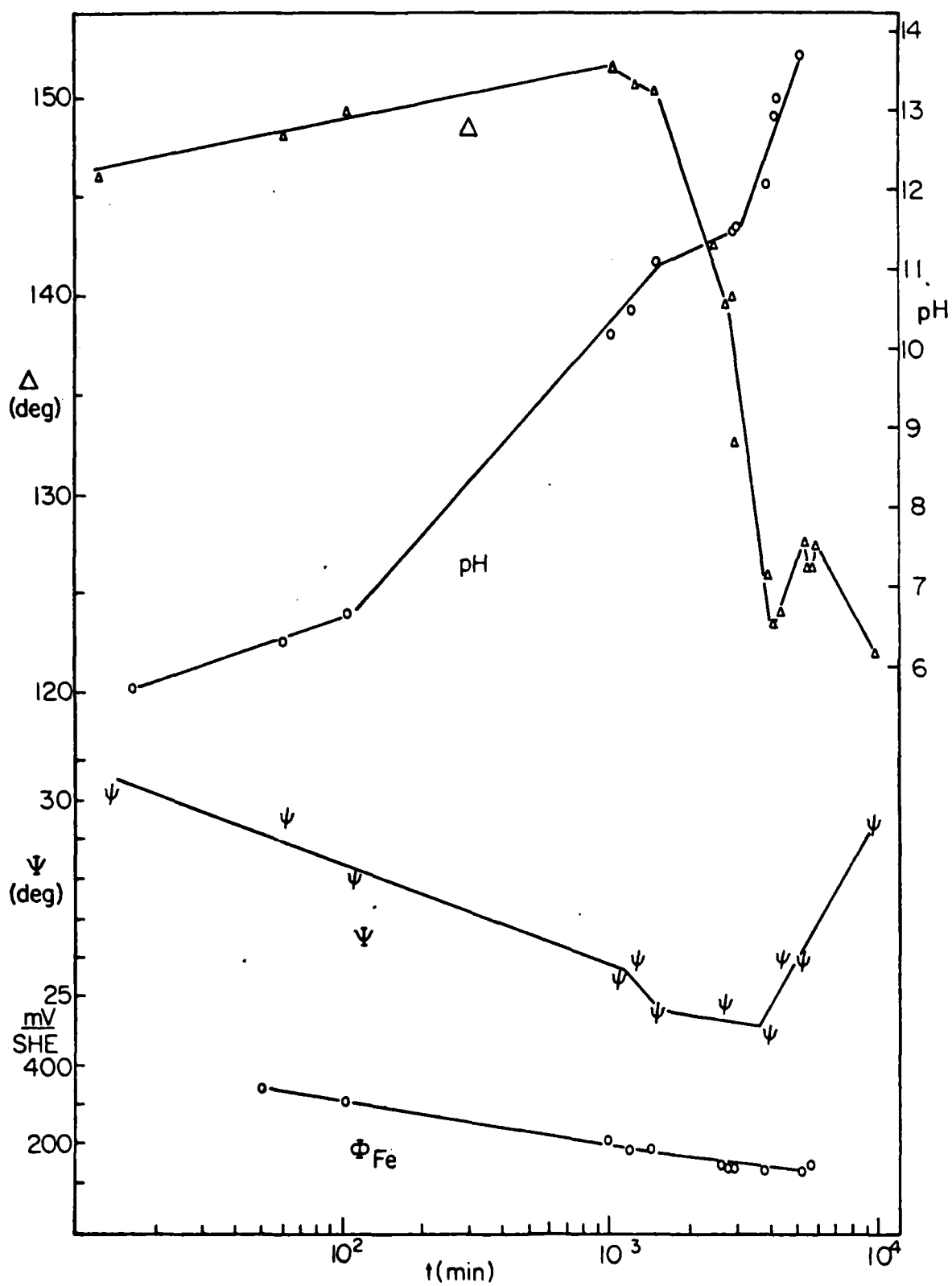
$$\lambda = 546.1 \text{ nm}$$

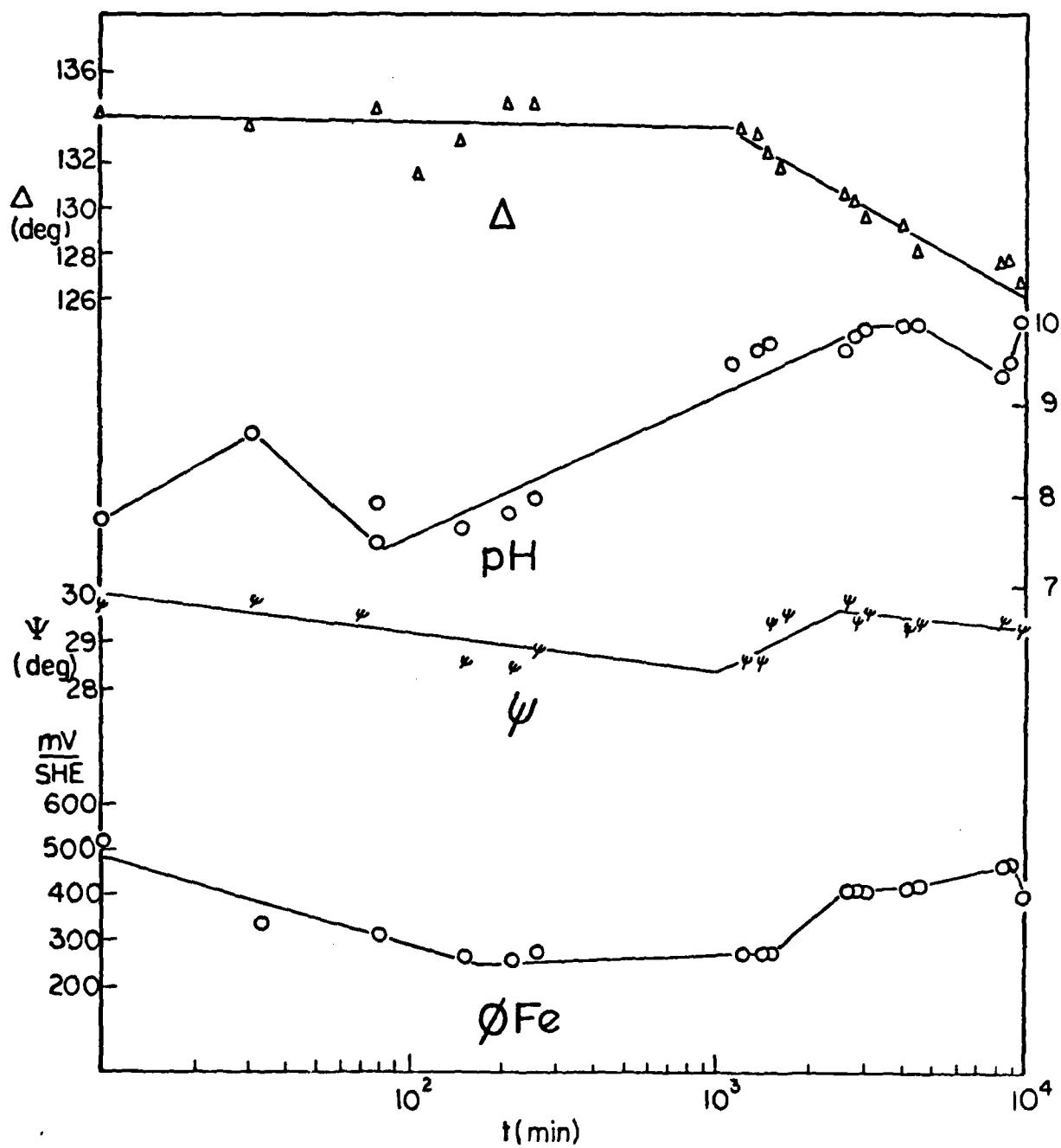
$$\Phi = 68^\circ$$











PART-II

Hydrogen Interactions with Stressed Titanium-Palladium Alloys and Stressed Vanadium Explored with Field Ion Microscopy

J. J. Carroll and A. J. Melmed
Surface Science Division

and

J. Kruger
Chemical Stability and Corrosion Division

National Bureau of Standards
Washington, D. C. 20234

ABSTRACT

Three titanium-palladium alloys, nominally containing one, two, and three at. % palladium, were prepared by vacuum annealing titanium wires that were previously electroplated with palladium thin films. Field ion micrographs obtained from these materials at temperatures less than 30 K indicated significant alloy inhomogeneities. In addition, the micrographs indicated that the alloys offered no greater resistance to hydrogen/stress induced crack formation and development than unalloyed titanium under similar conditions.

Field ion micrographs of 99.9+ percent pure vanadium showed surfaces having significant short-range disorder, an effect that might be due to imageable impurities. Experiments demonstrated that improved surface order is gained in the top-most layers by exposing specimens to hydrogen imaging conditions at temperatures less than 30 K. This hydrogen treatment leaves the ordered vanadium surfaces free of defects.

Hydrogen Interactions with Stressed Titanium-Palladium Alloys and Stressed Vanadium Explored with Field Ion Microscopy

J. J. Carroll and A. J. Melmed
Surface Science Division

and

J. Kruger
Chemical Stability and Corrosion Division

National Bureau of Standards
Washington, D. C. 20234

1. FORWARD

Field ion microscopy presents an atomic view of a multifaceted, metal surface. Images are obtained while the specimen, in contact with imaging gas, is subjected to appreciable stress brought about by the necessary electric field. The advantage of the technique is that it permits observation of a metal surface before, during and after exposure to the potentially corrosive gas, hydrogen, or to a more inert gas, neon, while the specimen is under stress. Thus, the occurrence of hydrogen/stress induced metal defects is determined readily. The following is a description of exploratory experiments with titanium-palladium alloys and vanadium carried out with a conventional field ion microscope, previously described [1].

2. TITANIUM-PALLADIUM ALLOYS

2.1. Introduction

It was learned more than twenty years ago [2] that one may improve the corrosion resistance of titanium in oxidizing and reducing acid media by several hundred-fold by alloying with small amounts of palladium. Improved corrosion resistance is accompanied by sharply increasing material hardness with increasing palladium contents of the alloy. The solubility of palladium in alpha titanium is slightly less than 3 at.% at room temperature [3], so relatively small amounts of the palladium

constituent have relatively large effects. In view of the previous success with field ion microscopy in observing the initial crack formation in the presence of stress and hydrogen with pure titanium [4], it is of interest to pursue the effects on titanium-palladium alloys, to evaluate their susceptibility to stress corrosion cracking due to hydrogen embrittlement with the field ion microscope, and to compare the results with those previously obtained with pure titanium [4].

2.2. Specimen Preparation

Three titanium-palladium alloys containing nominally 1, 2, and 3 at.% palladium were made by electroplating approximately 270, 530 and 800 nm thick palladium films, respectively, onto 0.013 cm diameter titanium wires, previously strain annealed in vacuum at approximately 1000 °C, and subsequently annealing the composite at 1000 °C for two hours and at 520 °C for about 17 hours. The titanium wire was originally characterized as 99.99+ percent pure, and was used in the previous field ion microscopy study of titanium [4], where it was found that strain annealing titanium wire markedly increased the average lifetime of specimens in the field ion microscope. The palladium electroplating bath contained 200 g PdCl_2 , about 100 g NH_4Cl , 3.8 g H_2O and enough HCl to bring the pH in the 0.1-0.5 range. The bath was held at about 40 °C and agitated. The electroplating was carried out at about 75 amps/m^2 using a stainless steel counter electrode. The electroplating bath was designed to electroplate palladium on metal more noble than titanium, and, as a consequence, titanium wires were cleaned prior to electroplating by a chemical dip into a bath containing 11 parts NiCl_2 , six parts HCl (conc.), and one part NH_4F . Ultimately, the alloy wires were electrolytically sharpened at about 50 V (dc) vs. a carbon rod cathode in a methanol

solution containing one percent HClO_4 and held at -50°C .

2.3. Results

Within the limitations of conventional field ion microscopy, where assessments of chemical identification are derived sometimes from qualitative differences in appearance among micrographs, it is concluded that the alloying procedure was not completely successful, i.e., although evidence from some specimens indicated the presence of titanium-palladium alloy, other specimens showed no evidence of alloy formation. Each of the three alloys were sampled by field ion microscopy several times. Field ion micrographs from all samples of titanium-1 at.% palladium alloy were indistinguishable in appearance from those obtained from pure titanium, showing characteristic cracking behavior and the usual crack depths of 10-15 layers. It is assumed that these samples corresponded to unalloyed titanium. Field ion micrographs obtained from samples of titanium-2 at.% and -3 at.% palladium alloys indicated that these preparations were of nonuniform composition in that micrographs from some samples showed clearly different pattern appearance than micrographs from other samples, which were indistinguishable from those obtained from pure titanium.

Micrographs obtained from the titanium-1 at.% palladium alloy preparation showed neon and hydrogen field ion patterns typical of those obtained from pure titanium [4]. Patterns obtained using neon imaging gas [Fig. 1(a)] have uniform spot intensity and contrast, overall, with the $(10\bar{1}1)$ type planes showing the most order, typical of neon field ion micrographs from titanium. Patterns obtained using hydrogen imaging gas [Fig. 1(b)] show several defects, crack-like in appearance, predominately in the $\langle 10\bar{1}0 \rangle$ - $\langle 1\bar{1}20 \rangle$ zone with the $(10\bar{1}1)$ type planes remaining

relatively defect free, again typical of hydrogen field ion micrographs from pure titanium. A lingering question remains, and is as follows. Are the micrographs of Figs. 1(a,b) from alloyed or unalloyed titanium? In the absence of atom-probe field ion microscopy [5] evidence the question can't be answered definitively. If the alloying procedure worked perfectly and produced the sought after titanium-1 at.% palladium alloy, then only one pattern spot in a hundred would be due to palladium. Perhaps the electronic structure of the alloy is not sufficiently different from pure titanium to alter its imaging characteristics from those of titanium. Perhaps the plating procedure deposited less than the desired quantity due to the less noble character of the titanium substrate than the more usual gold substrate. Such an alloy might not be detectable with the presently used qualitative field ion microscopy. Without some positive indication that the alloying procedure was successful, then we assume that it was not.

Field ion microscopy of titanium-2 at.% and -3 at.% palladium alloys showed clearly that these preparations were not uniform in composition. In addition to the usual looking neon and hydrogen field ion micrographs obtained from some samples of titanium-2 at.% and -3 at.% palladium, shown respectively in Figs. 2(a,b) and Figs. 3(a,b), other samples from each alloy showed marked differences in pattern contrast characteristics, and, in the titanium-3 at.% palladium alloy, both contrast and structural differences from ordinary titanium patterns. Specifically, a titanium-2 at.% palladium alloy sample showed evidence of material inhomogeneities in the early stages of imaging. Figure 4(a) shows a dimly imaged, ordered material having several crystal planes and a brightly imaged, disordered area of another material. Field evaporation

of the tip surface leaves only a few remaining atoms of the brightly imaged inclusion and the development of another brightly imaged area in the lower right region [Fig. 4(b)]. With further field evaporation, the brightly imaged material occupies a greater proportion of the tip's imaging surface [Figs. 4(c,d)] until, eventually, the entire tip area is comprised of the brightly imaged material [Fig. 4(e)]. There were no further changes in composition evident during the lifetime of this tip. The sequence of micrographs in Fig. 4 are related to a schematic diagram in Fig. 5 that indicates approximately a possible configuration of the two imaged phases. It is assumed that the more ordered material imaged in Fig. 4(a) is pure titanium and that the less ordered, more brightly imaged material, imaged partially in Fig. 4(a) and exclusively in Fig. 4(e), is the desired titanium-2 at.% palladium alloy.

Hydrogen ion microscopy revealed that the apparent titanium-2 at.% palladium alloy [Fig. 4(e)] has no greater resistance to cracking caused by the combination of hydrogen and stress than does pure titanium. The hydrogen field ion micrograph shown in Fig. 6(a) indicates severe crack development in the $\langle 11\bar{2}0 \rangle$ - $\langle 10\bar{1}0 \rangle$ zone along with the less effected $(10\bar{1}1)$ type plane areas, a pattern typical of pure titanium under the same imaging conditions. When the hydrogen imaging gas was removed from the microscope prior to imaging and field evaporating in neon, the crack development ceased and the number and severity of the imaged defects decreased upon continued field evaporation in the inert imaging gas. Figs. 6(b,c) are neon field ion micrographs of the previously attacked specimen [Fig. 6(a)] obtained after about three and twelve $(11\bar{2}0)$ planes field evaporated, respectively. Some defects remain [arrows, Fig. 6(c)] but, nevertheless, the appearance of the $\langle 11\bar{2}0 \rangle$ - $\langle 10\bar{1}0 \rangle$

zone has improved. The reproducibility of this experiment was established by reimaging the surface, previously neon field evaporated [Fig. 6(c)], in hydrogen. The hydrogen field ion micrograph of Fig. 6(d) shows the formation of crack-like defects, and the subsequent neon field ion micrographs of Figs. 6(e,f) show the alloy surface after six and sixteen (1011) planes have field evaporated. Figure 6(e) indicates that the crack-like features have disappeared. The brightly imaged cross area of the $\langle 11\bar{2}0 \rangle$ - $\langle 10\bar{1}0 \rangle$ and $\langle 11\bar{2}0 \rangle$ - $\langle 11\bar{2}2 \rangle$ zones clearly make the neon field ion micrographs from this alloy distinguishable from those of pure titanium [4]. The above evidence indicates that crystallographically specific attack of the titanium-2 at.% palladium alloy surface occurred by the corroding agent, hydrogen, in combination with metal tensile stress ($17 \times 10^9 \text{ N/m}^2$) and lead to stress corrosion cracking. The crack depths formed in this alloy were not significantly different from those formed in pure titanium [4]. Crack depths were estimated from a count of the number of nearby (1011) planes that were required to field evaporate in neon in order to cause the disappearance of defects that originated during previous hydrogen imaging.

Hydrogen field ion micrographs [Fig. 7(a)] obtained from an atypical specimen of titanium-3 at.% palladium alloy indicated that the material failed to exhibit the expected crack-like defects, and possibly might have a cubic crystal structure. The defects present in Fig. 7(a) appear to be less disruptive of the surface order than in other hydrogen field ion micrographs [Figs. 1(b), 2(b), 3(b), 6(a,d)]. Neon field ion micrographs [Fig. 7(b)] from this specimen show uniform contrast instead of local variations in contrast, a feature found in a titanium-2 at.% palladium alloy specimen. Assuming that this contrast feature would

prevail in the titanium-3 at.% palladium alloy then one may conclude that the imaged material, in this case, is either unalloyed palladium or titanium with a grain or twin boundary. The latter interpretation involves the identification of the three large planes in Fig. 7(a) as $(10\bar{1}1)$ type planes and one of the defects as a grain or twin boundary. If this is the case, then the especially effected $\langle 10\bar{1}0 \rangle - \langle 11\bar{2}0 \rangle$ zone is not imaged.

It is recognized that the above survey of these titanium-palladium alloys using field ion microscopy was limited by not assuring that the specimens were uniform in composition and homogeneous. There are significant uncertainties, as a result, regarding the chemical composition of the imaged material, i.e., titanium-palladium alloy, titanium, or palladium. In one important case of a titanium-2 at.% palladium specimen the results of hydrogen field ion microscopy were attributed clearly to a titanium-palladium alloy without knowledge of the alloy's precise composition.

3. VANADIUM

3.1. Introduction

Vanadium absorbs substantial quantities of hydrogen at elevated temperatures in hydrogen atmospheres and retains as much as 42 at.% hydrogen at room temperature [6], leading to hydrogen embrittlement [7]. Hydrogen absorption occurs at room temperature but may be inhibited by a monolayer of oxide [8]. In some cases [8,9] it is found that oxides and other surface impurities are difficult to remove, requiring heat treatments to within a few degrees of vanadium's melting point. Finally, there is atom-probe evidence [10] for the formation of vanadium-hydride ions in 10^{-6} Pa residual hydrogen at 21 K, indicating that a strong

vanadium-hydrogen interaction occurs under field ion microscopy conditions. In the following, experiments will be described that probe this interaction and its resultant effect on vanadium.

3.2. Sample Preparation

The vanadium source material was 99.9+ percent pure, zone refined {100} oriented single crystal rod from which several 5×10^{-4} m rods were spark cut with the {100} plane approximately perpendicular to the rod's axis. Two electropolishing steps were used to make sharp tips suitable for field ion microscopy. (1) The diameter of a rod was significantly reduced and the surface made shiny bright by electropolishing at 20 V (dc) in a 1:1 or 1:2 solution of perchloric acid (70 percent) and methanol. (2) The final polishing step, performed while observing the process at 150 magnification, used a 1:2 solution of HCl (conc.) and water at 2 V (ac). The electrolyte was contained in a loop of 0.13 mm platinum wire. An alternative step (2) procedure used a 1:3 solution of HNO_3 (conc.) and HF at 2 V (ac) without the aid of an optical microscope. Steps (1.) and (2.) were performed usually with the electrolyte near room temperature. Image quality was not effected, however, by using electrolyte (a) cooled from -30 to -50 °C. Methanol was used to rinse specimens at appropriate stages during tip manufacture.

3.3. Results

The appearance of neon field ion micrographs obtained from vanadium is dependent upon the specimen's recent history of exposure to hydrogen in the microscope, i.e., patterns obtained from a specimen previously exposed to hydrogen imaging conditions or to moderate hydrogen partial pressures are more ordered and show more crystal planes than patterns obtained with purer neon from a specimen not recently imaged with

hydrogen.

Directing attention to the appearance properties of the latter case first, the neon field ion micrographs shown in Fig. 8 were obtained from a specimen not previously imaged in hydrogen and with the microscope vacuum system especially gettered to reduce the base pressure to 10^{-8} Pa. The principle planes imaged are the central (100) and the four large {110} planes. The {111} planes were not imaged in this study. Other crystal plane areas appeared disordered. The {112} planes, for example, were expected to be moderately prominent in Fig. 8(a). Subsequent micrographs from this specimen indicated the presence of a thin plate of material, perhaps vanadium of different orientation, as shown in the fuzzy area in Fig. 8(b), and at substantially lower imaging voltage in Fig. 8(c). The plate boundaries are clearly defined. The specimen returned to its former appearance [Fig. 9(d)] following field evaporation sufficient to remove the plate imperfection. The micrographs of Figs. 8(b,c) are used to support the following conjecture concerning the origin of the fuzzy appearance of some atom spots, particularly pronounced in Fig. 8(a). Most imaging atoms of the plate appear fuzzy and unresolved in Fig. 8(b) because the plate may have slipped in the stress of the applied field and protruded sufficiently from the remaining hemispherically shaped cap surface. The resultant larger fields local to the protruding plate allow neon ionization to occur further away from the surface atoms, thus reducing the atomic resolution of the plate. Analogously, similar actions attributed to single atoms or groups of atoms--possibly impurities, within the vanadium matrix would account for the appearance of the occasional, lesser resolved spot, a characteristic found in the foregoing neon field ion micrographs from this material.

Exposing vanadium to hydrogen imaging conditions dramatically effects the appearance of neon field ion micrographs obtained subsequently, as demonstrated in Fig. 9. The hydrogen field ion micrograph shown in Fig. 9(a) was obtained with vanadium in an unstable, field evaporating condition, whereas, Fig. 9(b) was obtained under stable imaging conditions at lower fields. Notice that two of the $\{112\}$ planes are visible. The remaining micrographs in Fig. 9 were obtained with neon imaging gas after the hydrogen was pumped away while maintaining the field. The procedure minimizes surface contamination during imaging gas changes. Figures 9(c,d,e,f) were obtained after field evaporating less than a monolayer, one layer, three and five layers, respectively, from the central (100) plane. The $\{112\}$, $\{103\}$, and $\{115\}$ planes are fully resolved most clearly in Fig. 9(f). The vanadium field ion micrograph of Fig. 10 was obtained in a helium and neon gas mixture from another specimen preimaged in hydrogen. Helium tends to highlight the well ordered, high index plane areas near the central (100) plane.

It is interesting and informative to compare helium-neon field ion micrographs obtained from ordered vanadium [Fig. 10] and disordered vanadium [Fig. 11]. The specimen shown in Fig. 11 was not imaged previously in hydrogen. The brighter spots are scattered randomly across the imaged surface and the higher index areas near the central (100) plane are not highlighted as they are in Fig. 10. It is clear that an explanation involves the imageability of impurity atoms, present in Fig. 11, and not in Fig. 10, obscuring the overall crystal order. Hydrogen imaging appears to clean the imageable impurities from surface layers of vanadium. The conventional picture of the image process includes the thermal accommodation of imaging gas onto the surface through a series

of bounces. In addition to the other events of the imaging process, hydrogen may be absorbed by an active metal such as vanadium.

There is one question that is answered by the following experiment and it concerns whether hydrogen effects bulk cleaning or whether its effect is confined to a few surface layers. Ordered inert gas images obtained following hydrogen imaging conditions should be sustained with continued field evaporation if bulk cleaning is effected, or should be changed to disordered inert gas images if the effect is confined to a finite depth. Figures 12(a,b) correspond to images obtained using helium-neon and neon, respectively, from a specimen not previously exposed to hydrogen imaging conditions. They each show a lack of ordered $\{112\}$, $\{103\}$, and $\{105\}$ planes, which is characteristic of contaminated vanadium. Figure 12(a) shows scattered, non-ordered, highlighted areas and Fig. 12(b) shows the occasional fuzzy spot. Figure 12(c) shows a hydrogen image of the specimen and Fig. 12(d) shows the first subsequently obtained neon image, corresponding to the surface undergoing less than a monolayer of field evaporation following the hydrogen treatment. Notice that the four, square formed, darker lines connecting the $\{110\}$ planes in Fig. 12(c) are apparent in Fig. 12(d) but not in Fig. 12(e), obtained after field evaporating one (100) plane layer. They correspond to recessed areas formed by preferential field evaporation in hydrogen, about a layer deep in this case. Upon further field evaporation the micrographs of Figs. 12(f,g) were obtained after eleven and sixteen (100) plane layers, respectively. Notice that a deterioration of surface order has occurred after sixteen layers, but not a total obliteration. Compare Figs. 12(f,g). Imaging with a helium-neon mixture shows a more disordered surface [Fig. 12(h)] than

that from a probably purer vanadium specimen [Fig. 10], more order than from another vanadium specimen not exposed to hydrogen imaging conditions [Fig. 11], and approximately the same order as the starting conditions for the present specimen [Fig. 12(a)]. The effective penetration depth for hydrogen in this vanadium specimen, about sixteen layers, is in moderate agreement with depths found for hydrogen induced cracks in titanium [4] and palladium-titanium alloys. In this case, however, the interaction leaves the vanadium matrix free from crack defects.

As a side note, the normal imaging process was interrupted occasionally by momentary bursts in the rate of field evaporation with no apparent change in image quality. These events were observed using hydrogen, neon or helium-neon gas mixtures at liquid helium cooled temperatures and with neon at liquid nitrogen, a wide variety of imaging conditions. We suspect that during normal imaging and field evaporation there is an adsorbed film, probably involving hydrogen, that tends to stabilize the surface. We associate the momentary bursts in field evaporation rates with a corresponding removal of the adsorbed film which causes the surface to destabilize until the film is reformed.

It would be useful to carry out further atom-probe investigations directed toward chemically characterizing the above observations, and to perform vanadium field ion microscopy in a baked vacuum chamber in order to gain further insights into the hydrogen-vanadium interaction. If the conclusion that hydrogen exposures at low temperatures tend to clean the top few surface layers of vanadium is supported by the atom-probe, then the hydrogen exposure technique could be adapted to larger, single crystal vanadium studies where the attainment of a clean vanadium surface

proved to be a formidable achievement [8,9,11].

4. SUMMARY

Hydrogen field ion microscopy of titanium-palladium alloys at temperatures less than 30 K indicated that the alloys offer no greater resistance to the development of surface cracks in the $\langle 11\bar{2}0 \rangle$ - $\langle 10\bar{1}0 \rangle$ zone and the $(11\bar{2}0)$ and $(10\bar{1}0)$ plane areas, induced by the combination of hydrogen and stress, than does unalloyed titanium.

Field ion micrographs of 99.9+ percent pure vanadium showed surfaces having significant short-range disorder, an effect which was attributed to imageable impurities. Experiments demonstrated that improved surface order is gained in the top-most layers by exposing specimens to hydrogen imaging conditions at temperatures less than 30 K. This hydrogen treatment leaves the vanadium surfaces ordered and free of defects.

5. ACKNOWLEDGEMENTS

We recognize the assistance of John P. Young of the Chemical Stability and Corrosion Division who palladium plated titanium wire specimens, and of Francis S. Biancaniello of the Metal Science and Standards Division who vacuum annealed the palladium plated titanium specimens.

REFERENCES

- [1] J. J. Carroll, A. J. Melmed and J. Kruger, "The study of the early stages of hydrogen embrittlement of some metals and alloys using field ion microscopy", in: Passive Films, Surface Structure and Stress Corrosion and Crevice Corrosion Susceptibility, NBSIR 79-1904 (Navy), Part I, (November, 1979), pp. 1-26.
- [2] M. Stern and H. Wissenberg, "The influence of noble metal alloy additions on the electrochemical and corrosion behavior of titanium", J. Electrochem. Soc., 106 (1958) 759-764; L. F. Plock, "Titanium alloys for crevice corrosion resistance", RMI Report R&D 505, Reactive Metals, Inc., Niles, Ohio (1967).
- [3] H. Nisimura and T. Hiramatsu, J. Japan Inst. Metals, 22 (1968) 88.
- [4] J. J. Carroll, J. Smit and A. J. Melmed, "Field ion imaging of titanium and effects due to hydrogen", Surface Sci. 45 (1974) 640-648.
- [5] E. W. Müller and T. T. Tsong, Field Ion Microscopy; Principles and Applications (Elsevier, New York, 1969), pp. 130-134.
- [6] William Rostoker, The Metallurgy of Vanadium (John Wiley, New York, 1958), p. 50.
- [7] *ibid*, p. 136.
- [8] A. Benninghoven, K. H. Müller, C. Plog, M. Schemmer and P. Steffens, "SIMS, EID and flash-filament investigation of O₂, H₂, (O₂ + H₂) and H₂O interaction with vanadium", Surface Sci. 63 (1977) 403-416.
- [9] T. W. Haas, A. G. Jackson and M. D. Hooker, "Adsorption on niobium (110), tantalum (110), and vanadium (110) surfaces, J. Chem. Phys. 46 (1967) 3025-3033.
- [10] E. W. Müller and S. V. Krishnaswamy, "Atom-probe FIM studies of vanadium, rhenium, and a copper-beryllium alloy", Phys. Stat. Sol. (A) 3 (1970) 27-31.
- [11] K. K. Vijai and P. F. Packman, "Gas adsorption studies on the (100) plane of vanadium by low-energy electron diffraction", J. Chem. Phys. 50 (1969) 1343-1349.

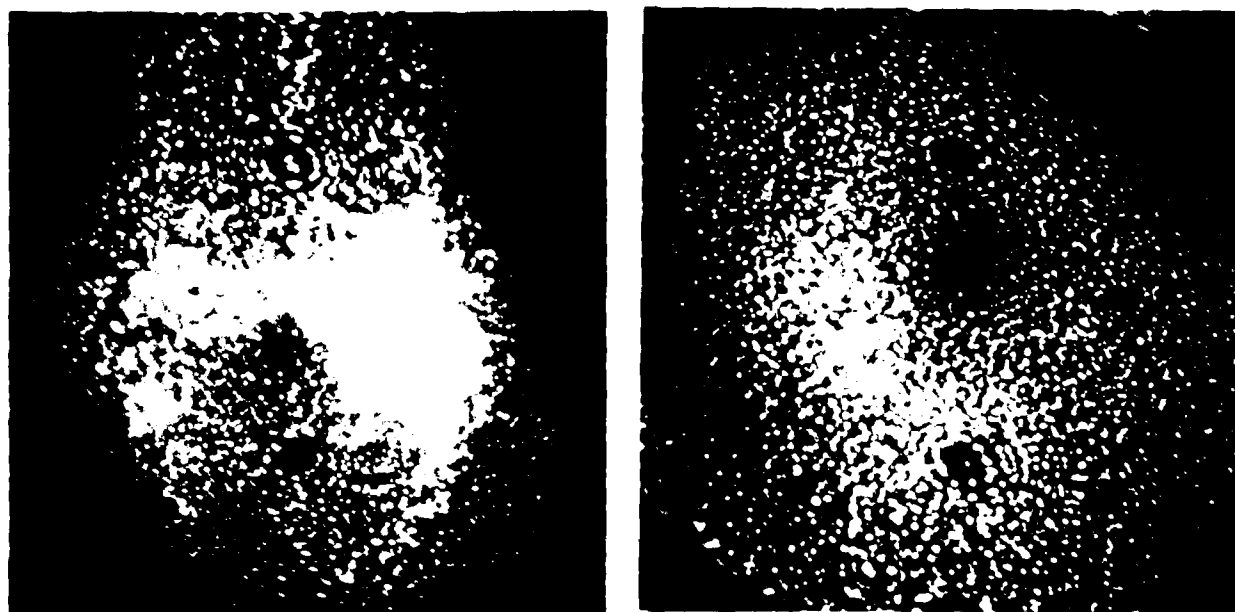


Figure 1. Electron micrographs of the same area of the
palladium
deposited on the surface of the palladium.

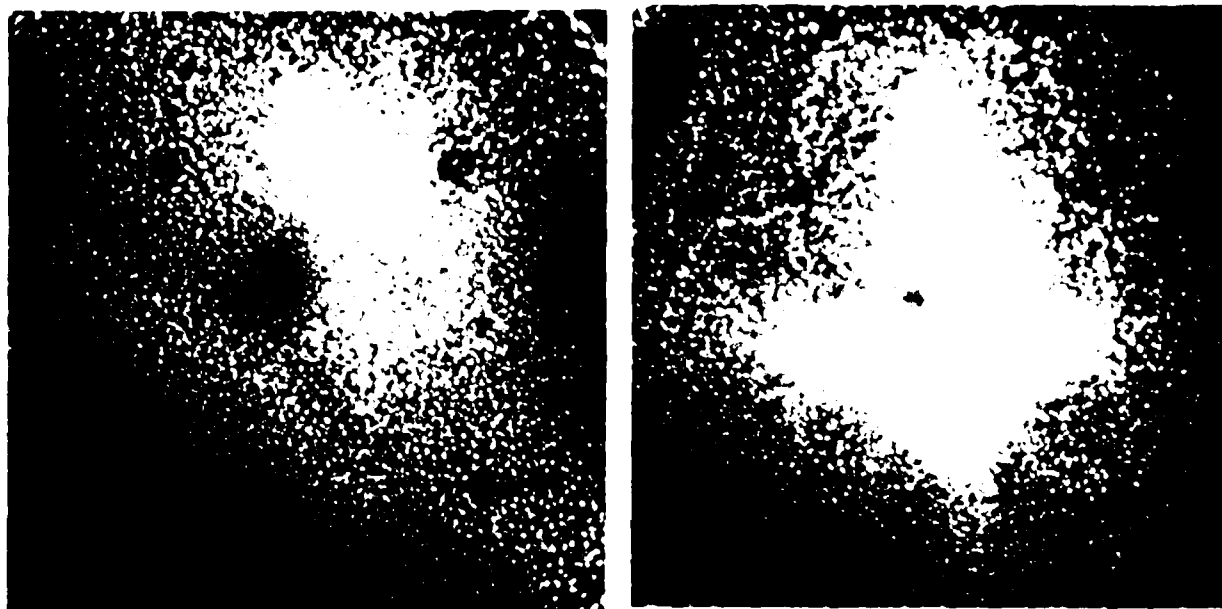
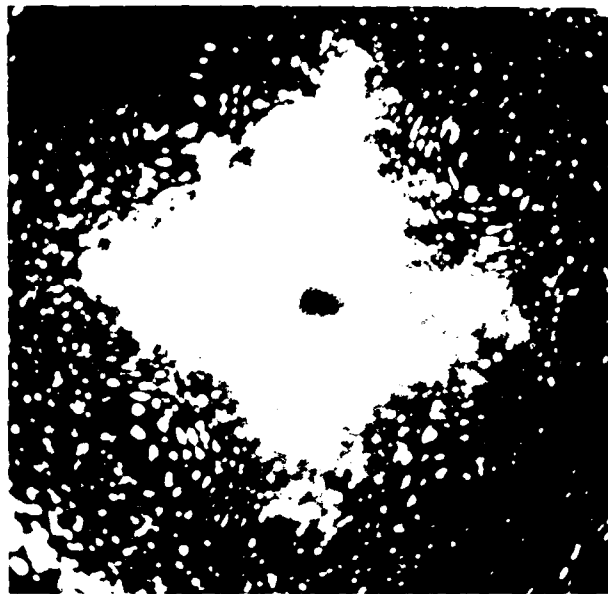
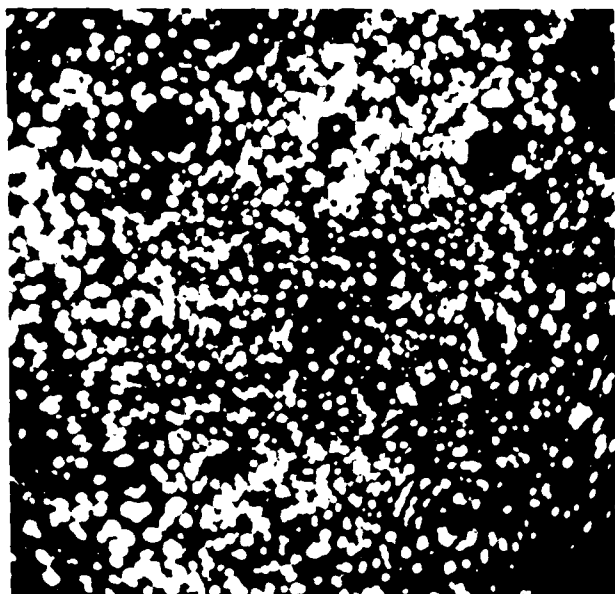
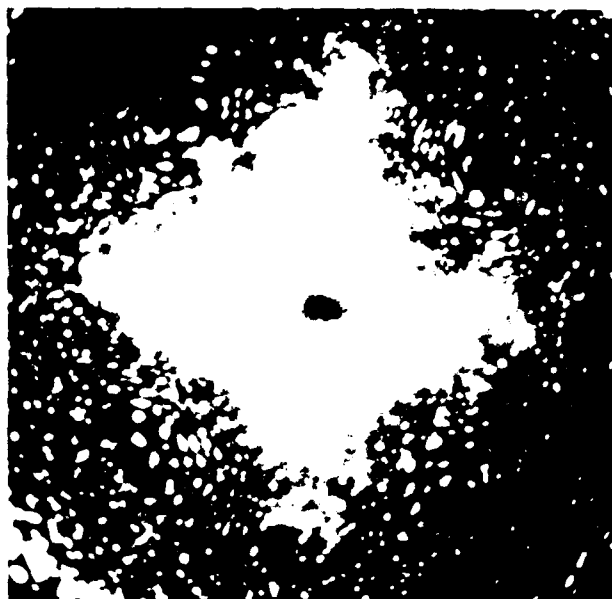
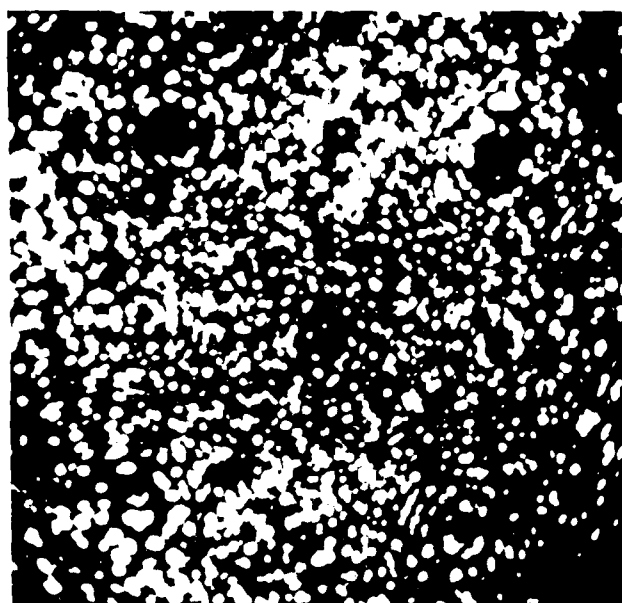
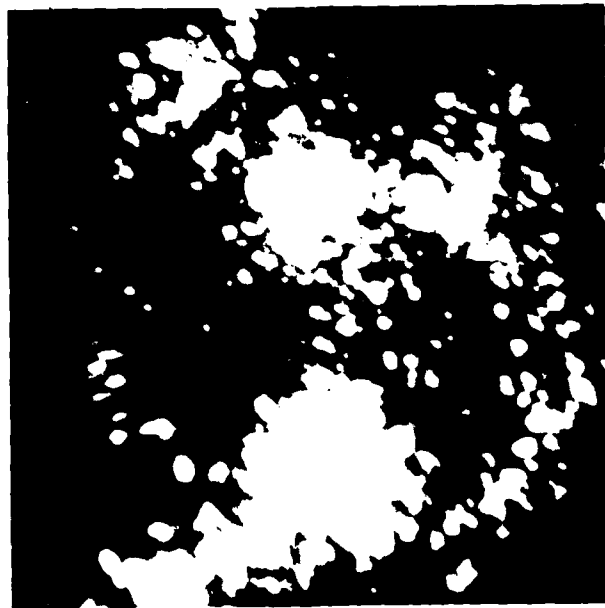
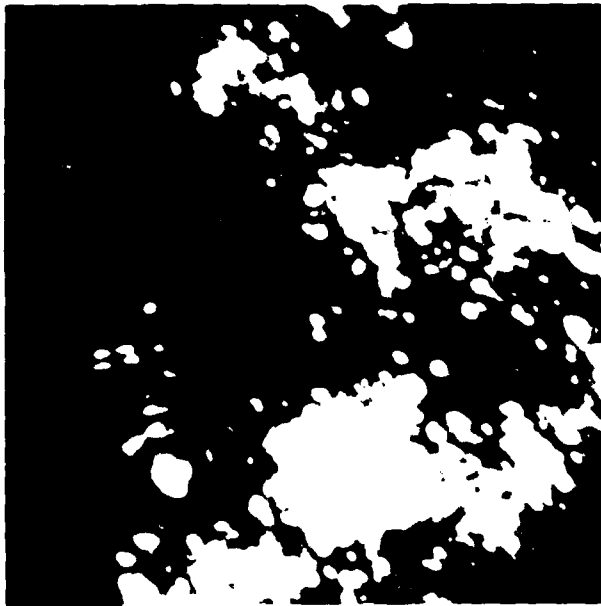
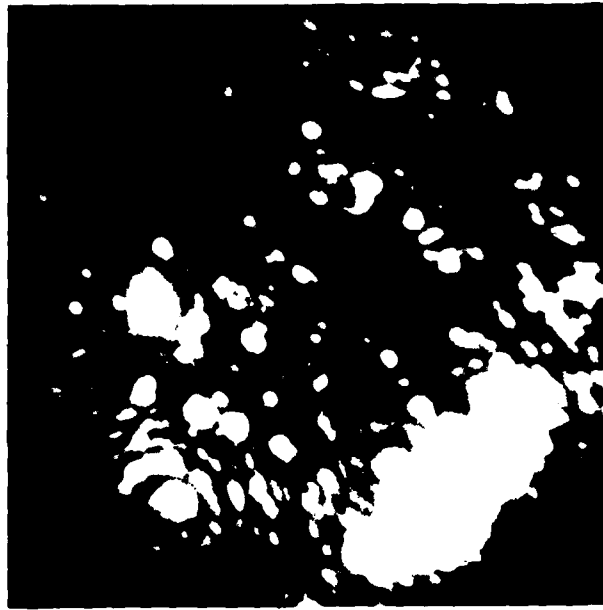
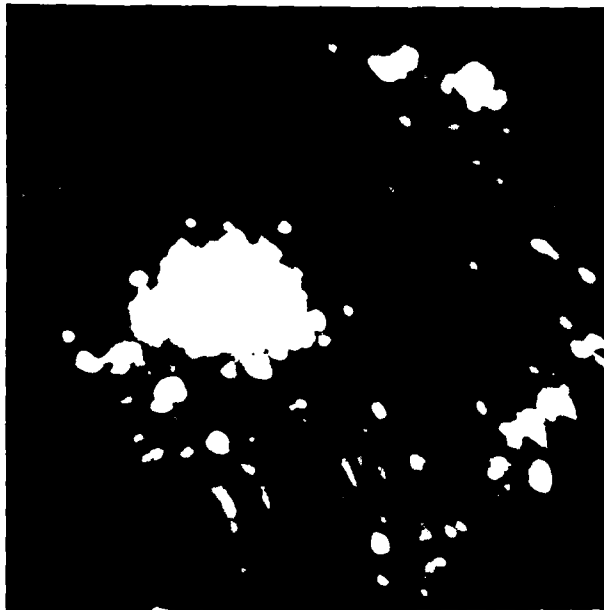


Figure 2 Field ion micrographs obtained from titanium-2 at
palladium.
(a) neon, 21.5 kV, 30 k; (b) hydrogen 15.1 kV, 30 k.







These four micrographs show the same field of view as the first four, but at a higher magnification. The large, bright, irregularly shaped mass in the center is more prominent, and the smaller, bright, circular or oval structures are more numerous and clearly defined.

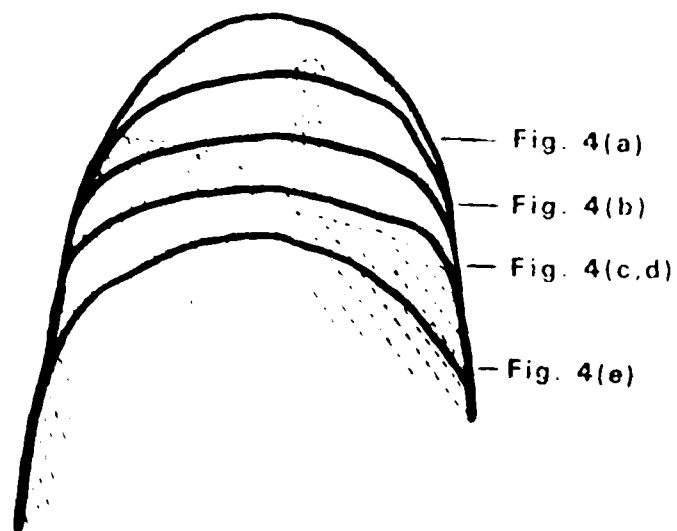
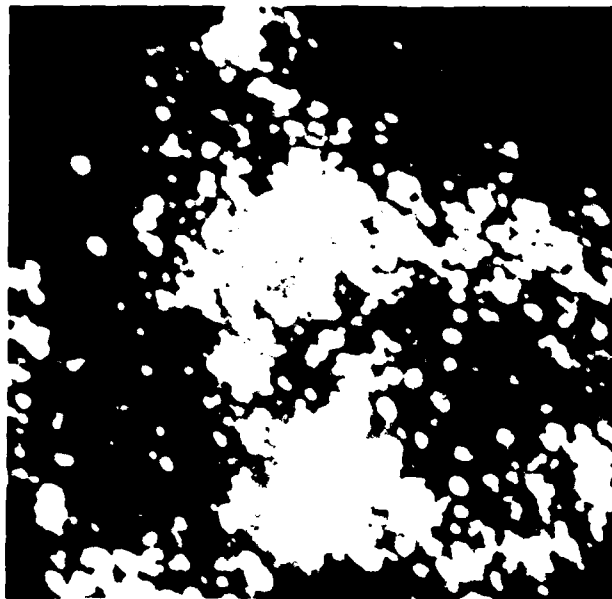


Figure 5 A cross-sectional schematic diagram of the two-phase specimen imaged in Figure 4.



Figure 1. Consecutive field ion micrographs obtained from a ^{223}Rn -contaminated palladium specimen that show evidence of hydrogen-induced surface crack formation. (a) hydrogen, 6.7 kV, 20 kV/cm; (b) hydrogen, 6.7 kV, 20 kV/cm; (c) neon, 8.6 kV, 30 kV/cm; (d) hydrogen, 6.7 kV, 20 kV/cm.

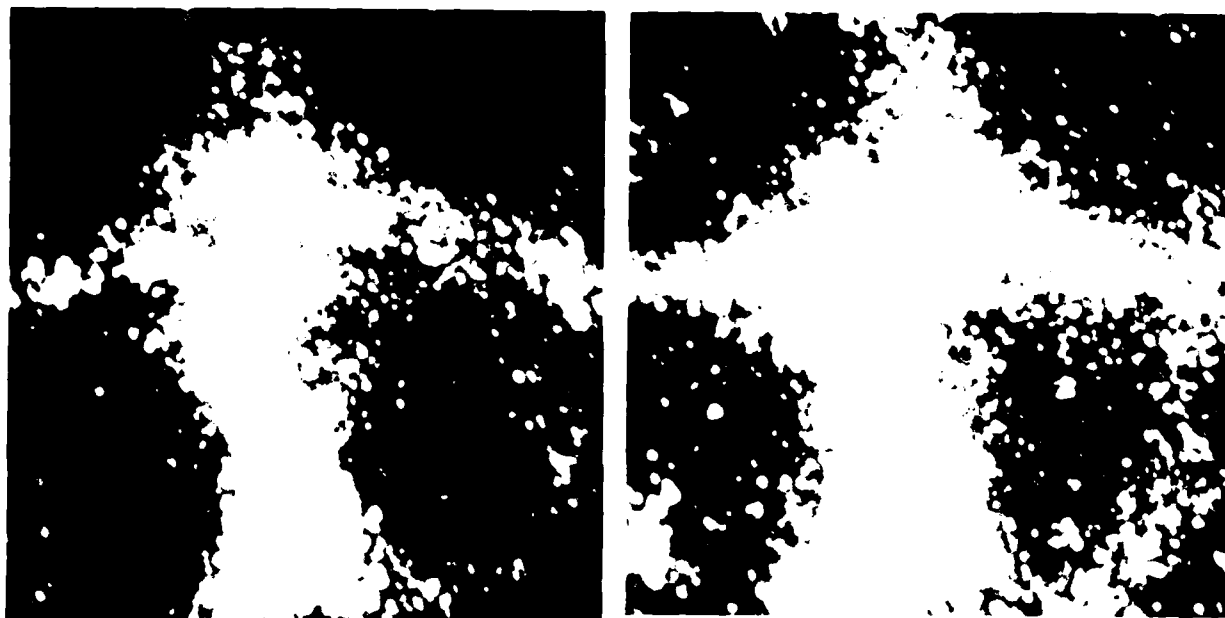


Figure 6. Field ion micrographs of tungsten tip.

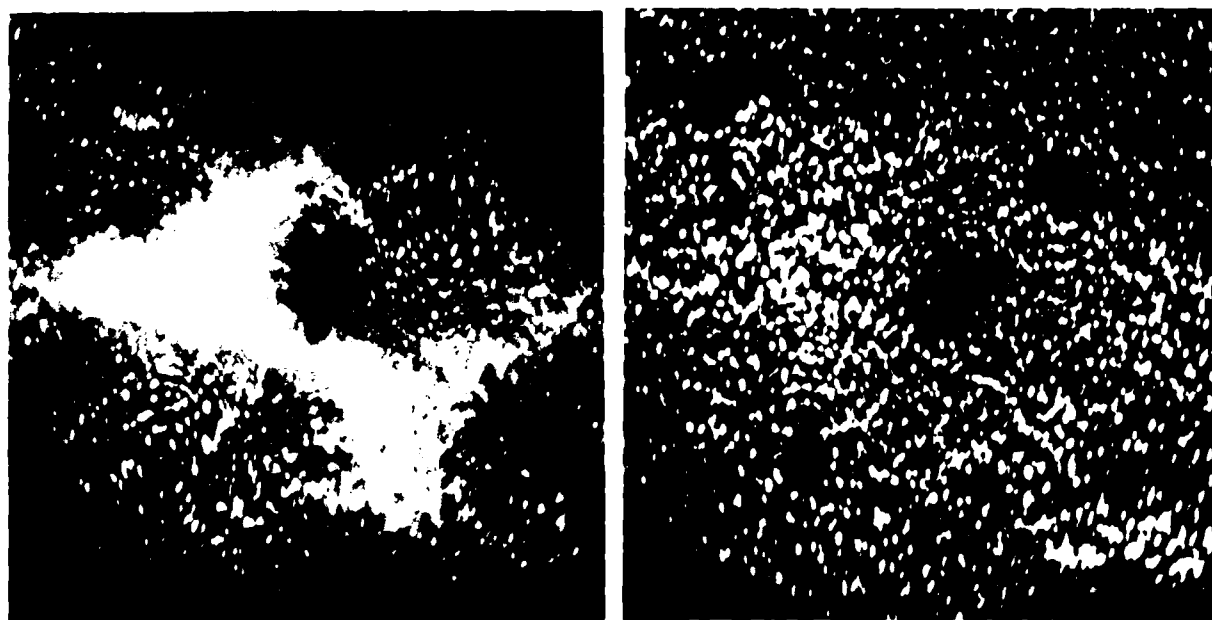


Figure 7. Field ion micrographs obtained from an atypical specimen of titanium-3 at. % palladium alloy. (a) hydrogen, 11 kV, 30 K; (b) neon, 16 kV, 30 K.

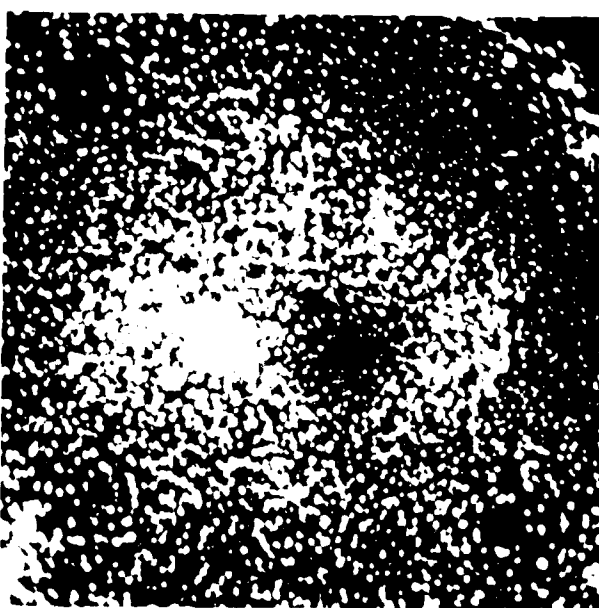
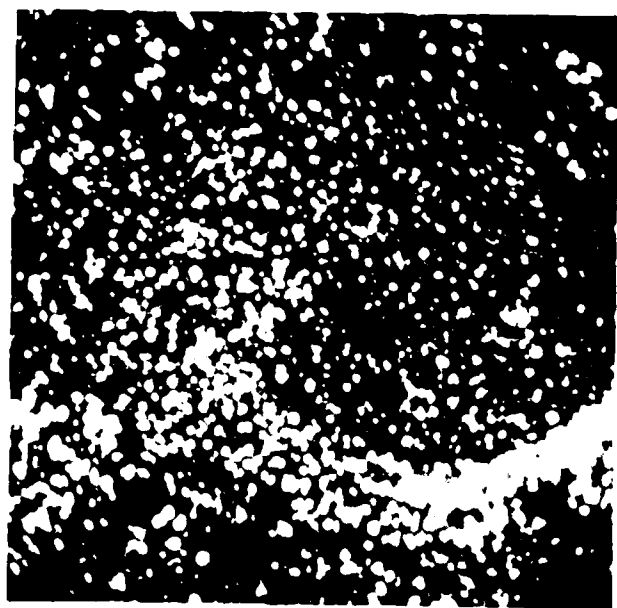
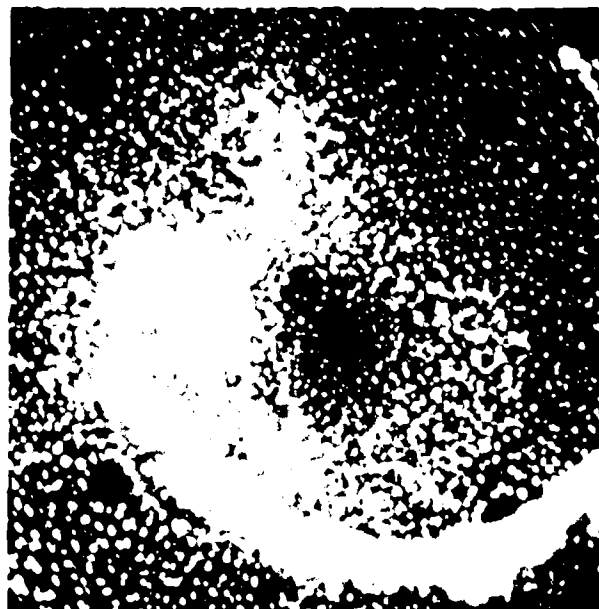
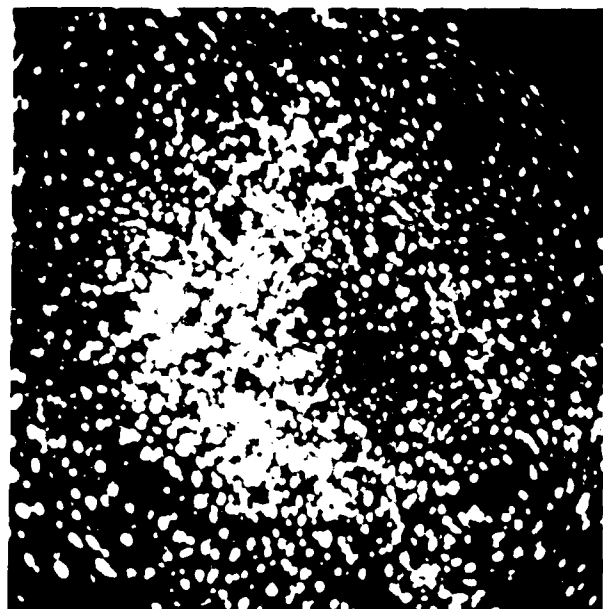


Figure 1. Neon field ion micrographs, obtained from vanadium tip, not treated previously with hydrogen. (a) 11.5 kV, (b) 12.5 kV, (c) 16.4 kV, (d) 18.5 kV.

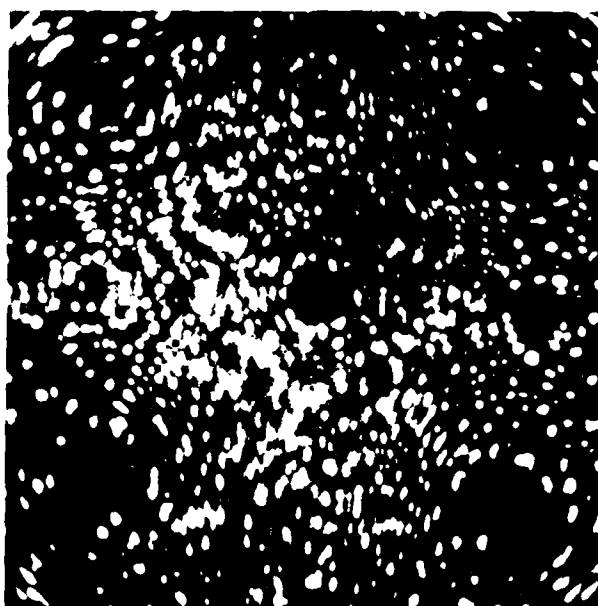
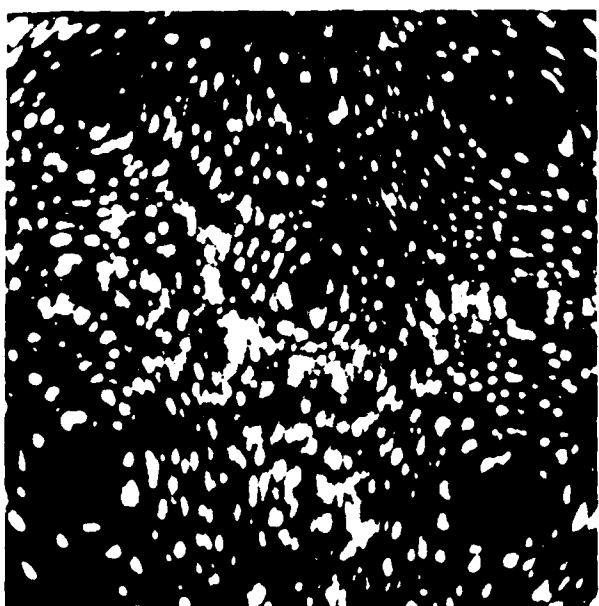
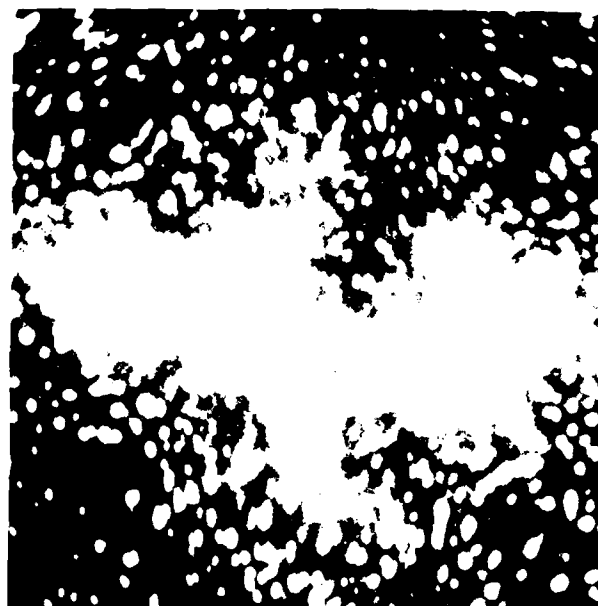


Figure 1. Consecutive field ion micrographs obtained from a single tungsten electrode that, after annealing with hydrogen, had a radius of 100 Å. Micrographs obtained subsequently at: (a) hydrogen, 7.4 kV, 3.0 × 10⁻⁶ Torr; (b) hydrogen, 6.3 kV, 3.0 × 10⁻⁶ Torr; (c) hydrogen, 11.5 kV, 3.0 × 10⁻⁶ Torr; (d) hydrogen, 13.4 kV, 3.0 × 10⁻⁶ Torr.

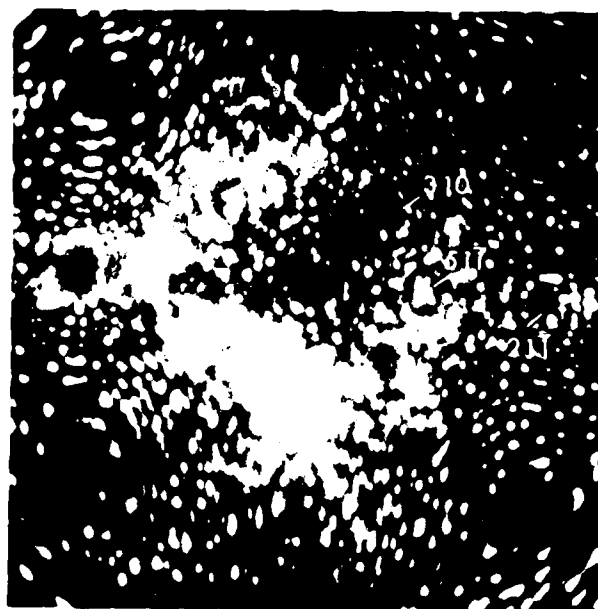
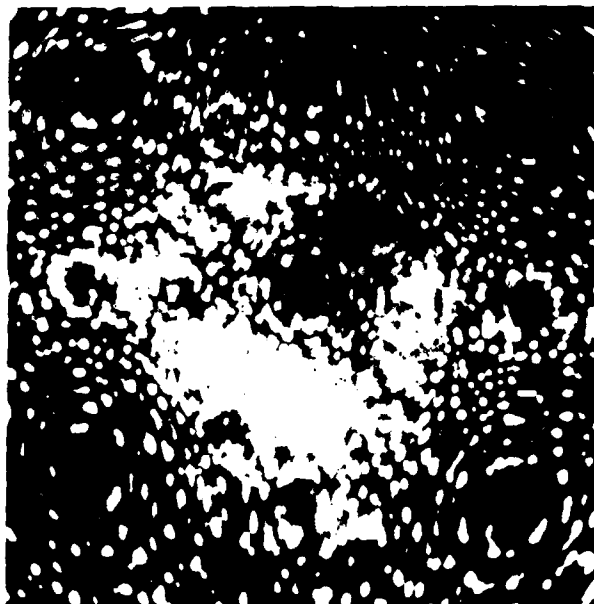


Figure 4 (e) and (f) neon, 12 kV, 30 f.



Figure 10. Helium-neon field ion micrograph obtained from vanadium previously irradiated with hydrogen, 10 kV, 100 k.

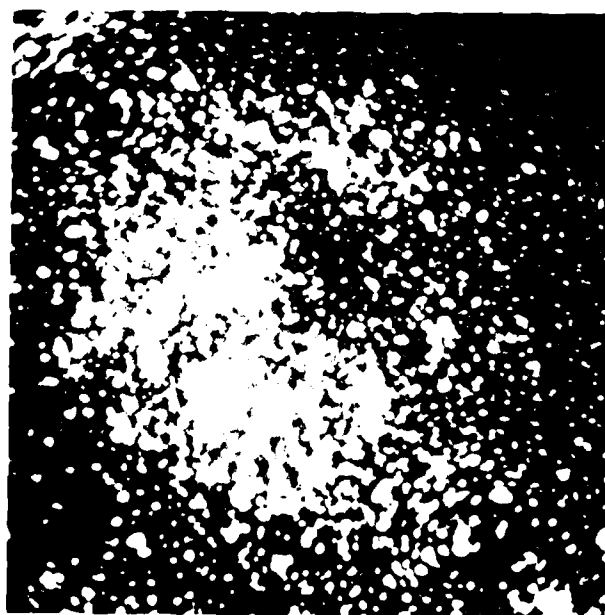


Figure 11. Helium-neon field ion micrograph obtained from vanadium not irradiated previously with hydrogen, 10 kV, 100 k.

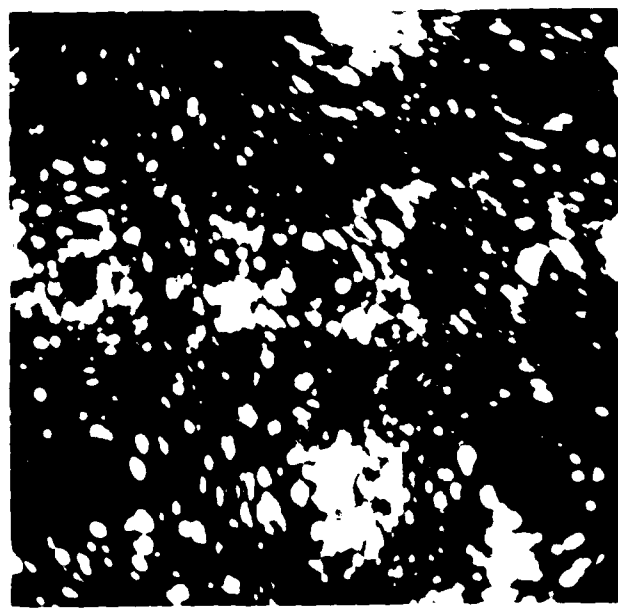
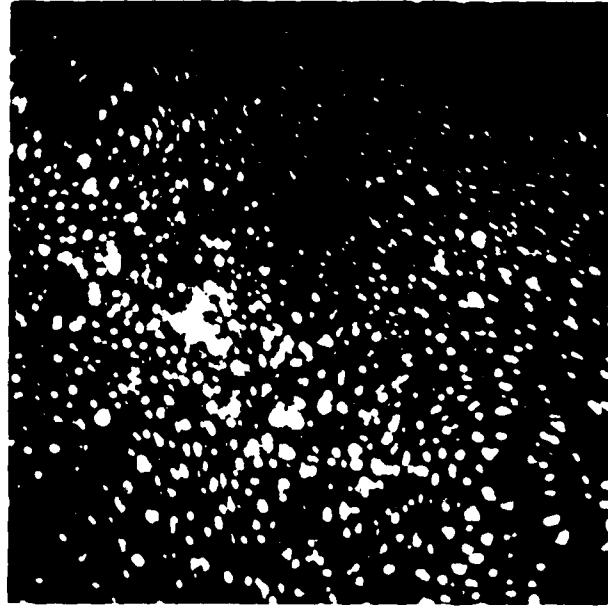
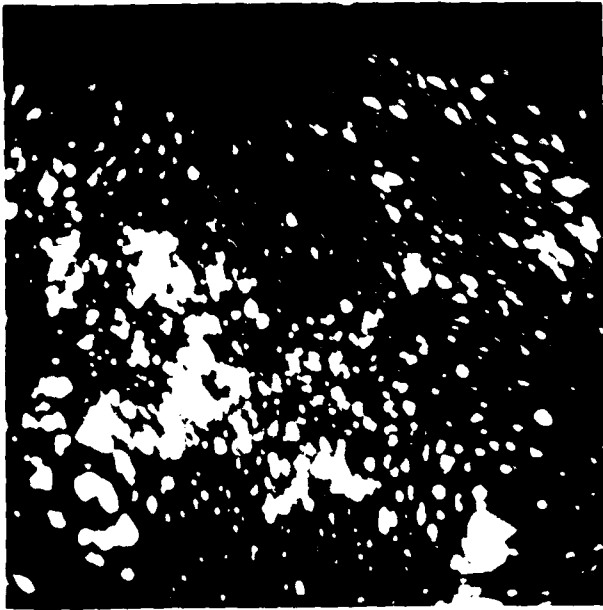


Figure 1. (a) Micrograph of field non-spherical particles of size 1-2 μ m, (b) micrograph of field non-spherical particles of size 2-3 μ m, (c) micrograph of field non-spherical particles of size 3-4 μ m, (d) micrograph of field non-spherical particles of size 4-5 μ m.

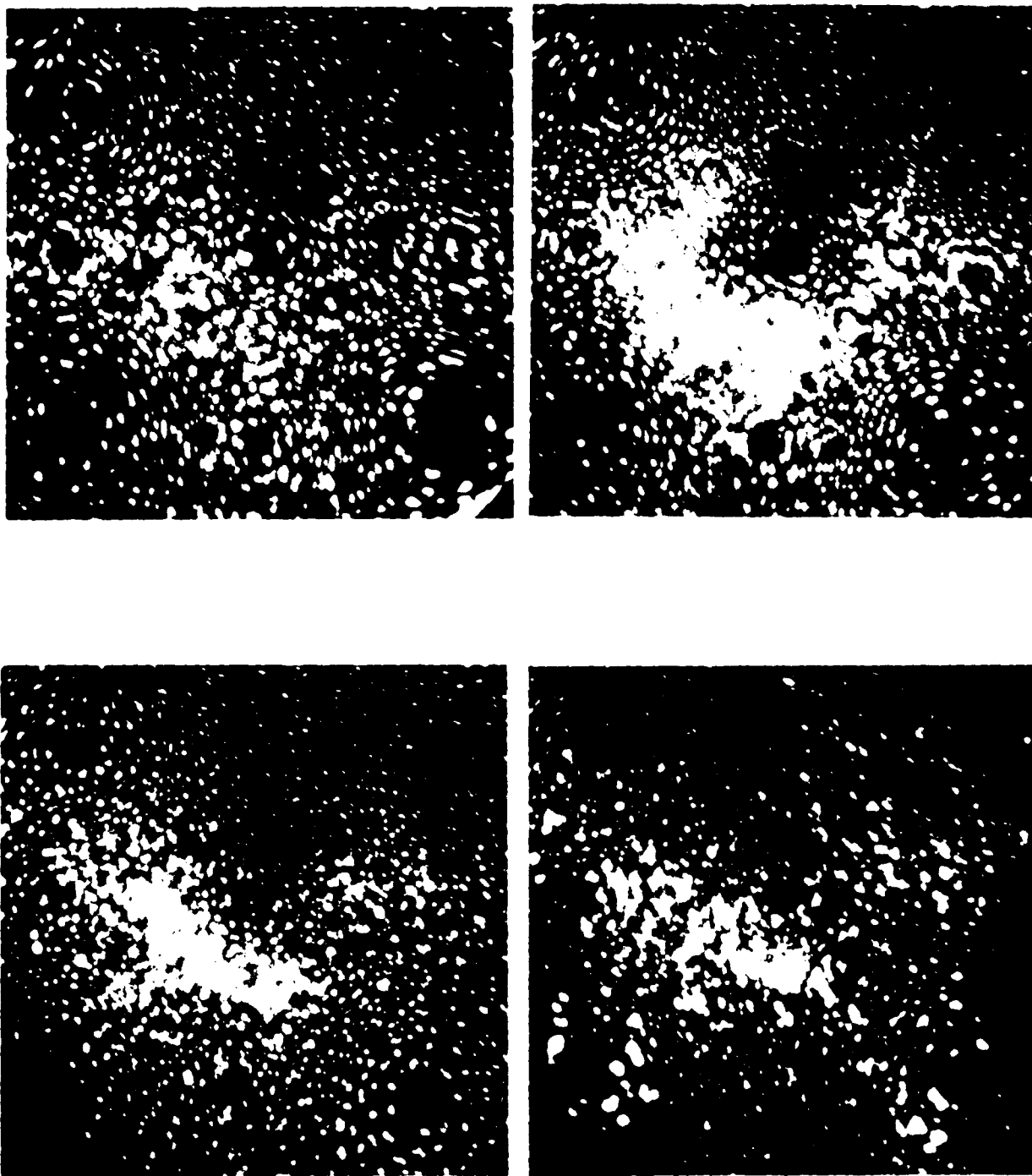


Figure 12 (e) neon, 12.5 kV, 30 F; (f) neon, 13.2 kV, 30 F;
 (g) neon, 14 kV, 30 F; (h) helium-neon, 14 kV, 30 F.

FILM

04-